

1 **Assessing improvements in global ocean pCO₂ machine learning reconstructions with**
2 **Southern Ocean autonomous sampling**

3 Thea H. Heimdal¹, Galen A. McKinley¹, Adrienne J. Sutton², Amanda R. Fay¹, Lucas Gloege³

4 ¹Columbia University and Lamont-Doherty Earth Observatory, Palisades, NY, USA

5 ²Pacific Marine Environmental Laboratory, National Oceanic and Atmospheric Administration,
6 Seattle, WA, USA

7 ³Open Earth Foundation, Marina del Rey, CA, USA

8 *Correspondence to:* Thea H. Heimdal (theimdal@ldeo.columbia.edu)

9

10 **Abstract**

11 The Southern Ocean plays an important role in the exchange of carbon between the atmosphere
12 and oceans, and is a critical region for the ocean uptake of anthropogenic CO₂. However, estimates
13 of the Southern Ocean air-sea CO₂ flux are highly uncertain due to limited data coverage. Increased
14 sampling in winter and across meridional gradients in the Southern Ocean may improve machine
15 learning (ML) reconstructions of global surface ocean pCO₂. Here, we use a Large Ensemble
16 Testbed (LET) of Earth System Models and the pCO₂-Residual reconstruction method to assess
17 improvements in pCO₂ reconstruction fidelity that could be achieved with additional autonomous
18 sampling in the Southern Ocean added to existing Surface Ocean CO₂ Atlas (SOCAT)
19 observations. The LET allows for a robust evaluation of the skill of pCO₂ reconstructions in space
20 and time through comparison to ‘model truth’. With only SOCAT sampling, Southern Ocean and
21 global pCO₂ are overestimated, and thus the ocean carbon sink is underestimated. Incorporating
22 Uncrewed Surface Vehicle (USV) sampling increases the spatial and seasonal coverage of
23 observations within the Southern Ocean, leading to a decrease in the overestimation of pCO₂. A
24 modest number of additional observations in southern hemisphere winter and across meridional
25 gradients in the Southern Ocean leads to improvement in reconstruction bias and root-mean
26 squared error (RMSE) by as much as 95 % and 16 %, respectively, as compared to SOCAT
27 sampling alone. Lastly, the large decadal variability of air-sea CO₂ fluxes shown by SOCAT-only
28 sampling may be partially attributable to undersampling of the Southern Ocean.

29

30 1. Introduction

31 The ocean plays an important role in mitigating climate change by sequestering anthropogenic
32 carbon emissions. From 1850 to 2023, the oceans have removed a total of 180 ± 35 Gt of carbon
33 (Friedlingstein et al., 2023). In order to fully understand the climate impacts from rising emissions,
34 it is essential to accurately quantify the air-sea CO_2 flux and the global ocean carbon sink in space
35 and time. The Surface Ocean CO_2 Atlas (SOCAT; Bakker et al., 2016) is the largest global
36 database of surface ocean CO_2 observations, with data starting in 1957. The main synthesis and
37 gridded products contain over 33 million high-quality direct shipboard measurements of $f\text{CO}_2$
38 (fugacity of CO_2) with an uncertainty of $< 5 \mu\text{atm}$ (Bakker et al., 2022). However, due to limited
39 resources for ocean observing, limited number of ships/routes, inaccessible regions and unsafe
40 waters, the database covers only about 1% of the global ocean at monthly $1^\circ \times 1^\circ$ spatial resolution
41 over the period of 1982-2023, and is highly biased towards the northern hemisphere.

42 Mapping methods have been developed to estimate full-coverage surface ocean $p\text{CO}_2$
43 across space and time by extrapolating to global coverage from these sparse SOCAT observations
44 (e.g., Landschützer et al., 2014; Rödenbeck et al., 2015; Gloege et al., 2022; Bennington et al.,
45 2022a,b). Most of these data products utilize machine learning (ML) algorithms to estimate a non-
46 linear function between a suite of driver variables (i.e., sea surface temperature - SST, sea surface
47 salinity - SSS, mixed layer depth - MLD, Chlorophyll - Chl-a, $x\text{CO}_2$ - atmospheric CO_2) and
48 surface ocean $p\text{CO}_2$ (the target variable) where these are co-located. The driver variables are
49 proxies for processes influencing ocean $p\text{CO}_2$. Full-coverage driver variable datasets are then
50 processed through these ML algorithms to produce estimated global full-coverage surface ocean
51 $p\text{CO}_2$. Since the data products rely on $p\text{CO}_2$ observations to estimate functions between the target
52 and driver variables, data sparsity remains a fundamental limitation to this technique.

53 It has been suggested that targeted sampling from autonomous platforms combined with
54 ships, filling in the state space of $p\text{CO}_2$, represents a path forward to improve surface ocean $p\text{CO}_2$
55 reconstructions (Bushinsky et al., 2019; Gregor et al., 2019; Gloege et al., 2021; Djeutchouang et
56 al., 2022; Landschützer et al., 2023; Hauck et al., 2023). One major obstacle, however, is that the
57 indirect $p\text{CO}_2$ estimates from floats have high uncertainties ($\pm 11.4 \mu\text{atm}$) and may be biased by
58 as much as $\sim 4 \mu\text{atm}$ (Bakker et al., 2016; Williams et al., 2017; Fay et al., 2018; Gray et al., 2018;
59 Sutton et al., 2021; Mackay and Watson 2021; Wu et al 2022). These large uncertainties and biases

60 arise when $p\text{CO}_2$ is not measured directly as in the observations included in SOCAT, but is rather
61 estimated using measurements of pH combined with a regression-derived alkalinity estimate
62 (Williams et al., 2017; Gray et al., 2018). SOCAT includes only direct $p\text{CO}_2$ observations. Biases
63 and uncertainties may have large impacts on global air-sea CO_2 flux estimates, given that the global
64 mean air-sea disequilibrium is only 5-8 μatm (McKinley et al., 2020). It is therefore critical that
65 bias and uncertainty corrections are well-constrained over different oceanic conditions and over
66 time.

67 Uncrewed Surface Vehicles (USVs), such as those manufactured and maintained by
68 Saildrone Inc., represent a new type of autonomous platform that can obtain direct $p\text{CO}_2$
69 observations with significantly lower uncertainties compared to other autonomous methods, and
70 equivalent to the highest-quality shipboard measurements contained in SOCAT ($\pm 2 \mu\text{atm}$; Sabine
71 et al., 2020; Sutton et al., 2021). Such improvements in sampling are critically important in the
72 undersampled Southern Ocean. This region is fundamental in terms of the ocean's ability to
73 remove carbon from the atmosphere, being responsible for $\sim 40\%$ of the global ocean uptake of
74 anthropogenic CO_2 (Khatiwala et al., 2009). Improved data coverage in the Southern Ocean
75 represents thus a major opportunity to advance our understanding of the global ocean carbon sink
76 (Lenton et al., 2006, 2013; Takahashi et al., 2009; Monteiro et al., 2015; Gregor et al., 2019; Gray
77 et al., 2018; Mongwe et al., 2018; Bushinsky et al., 2019; Sutton et al., 2021; Long et al., 2021;
78 Mackay et al., 2022; Wu et al., 2022; Landschützer et al., 2023; Hauck et al., 2023). A combination
79 of SOCAT and Saildrone USV observations would include high-accuracy data from both the long
80 record and global coverage of ship tracks, and the expanded finer resolution of spatial and seasonal
81 coverage of the poorly sampled Southern Ocean. Importantly, Saildrone USVs are also able to
82 cover the spatial extent and seasonal cycle of the meridional gradients, which has been shown to
83 be critical in order to reduce errors in reconstructing surface ocean $p\text{CO}_2$ (Djeutchouang et al.,
84 2022). A combined approach, with autonomous samples such as those obtained from Saildrone
85 USVs, in addition to high-quality observations collected from ships, represents thus a promising
86 solution to improve surface ocean $p\text{CO}_2$ ML reconstructions.

87 Here, we assess to what extent surface ocean $p\text{CO}_2$ reconstructions can improve by
88 implementing the $p\text{CO}_2$ -Residual machine learning (ML) reconstruction (Bennington et al., 2022a)
89 with the combined inputs of SOCAT and Saildrone USV coverage. However, instead of using real-

90 world observations, we sample the target (i.e., surface ocean pCO₂) and driver variables (i.e., SST,
91 SSS, MLD, Chl-a and xCO₂) from our Large Ensemble Testbed (LET) of Earth System Models
92 (ESMs) (e.g., Stamen et al., 2020; Gloege et al., 2021; Bennington et al., 2022a). There are two
93 major benefits of using a testbed compared to actual observations. First, in an ESM, the surface
94 ocean pCO₂ field is provided precisely at all model times and 1°x1° points. Therefore, the pCO₂
95 reconstructed by the ML algorithm can be robustly evaluated in space and time against a known
96 ‘truth’ (i.e., ‘model truth’). The reconstruction evaluation is thus not limited to the availability of
97 sparse real-world ocean observations. Secondly, a testbed can be used to plan and evaluate the
98 impact of different sampling strategies on the reconstructed pCO₂. It is important to stress that, by
99 using a model testbed, we do not predict real-world surface ocean pCO₂ and air-sea CO₂ fluxes.
100 The goal here is to assess the accuracy with which an ML algorithm can reconstruct the ‘model
101 truth’ given inputs of samples consistent with real-world data coverage from the SOCAT database
102 and Saildrone USVs.

103 By utilizing the observational coverage of SOCAT and Saildrone USV transects, we assess
104 to what extent the pCO₂-Residual method accurately reconstructs model surface ocean pCO₂ in
105 space and time. We test the impact of two different USV Southern Ocean sampling schemes, the
106 first based on a sampling campaign completed in 2019 (Sutton et al., 2021), and the second on
107 logistically feasible potential future meridional sampling. Additionally, we explore the timing,
108 magnitude, duration and spatial extent of Southern Ocean USV sample additions that most
109 significantly improve the pCO₂ predictions. Combined, the sampling patterns tested here
110 complements previous studies exploring the impact of additional sampling in the Southern Ocean
111 based on idealized full global coverage of floats, and float observations from recent deployments,
112 including the Southern Ocean Carbon and Climate Observations and Modeling (SOCCOM)
113 project, moorings and sailboats (Bushinsky et al., 2019; Denvil-Sommer et al., 2021;
114 Djetchouang et al., 2022; Hauck et al., 2023; Behncke et al., 2024; Landschützer et al., 2023).

115

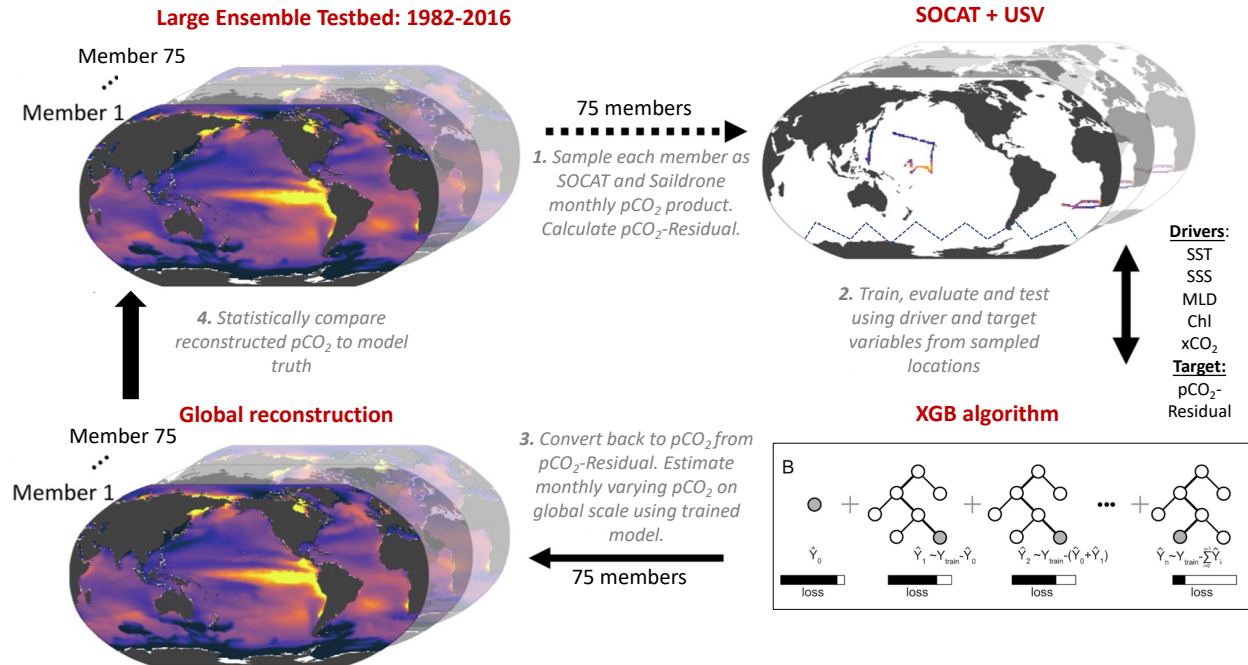
116 **2. Methods**

117 *2.1 The Large Ensemble Testbed (LET)*

118 In this study, the Large Ensemble Testbed (LET) includes 25 members from three independent
119 initial-condition ensemble models (i.e., CanESM2, CESM-LENS and GFDL-ESM2M; Kay et al.,
120 2015; Rodgers et al., 2015; Fyfe et al., 2017), giving a total of 75 members within the testbed. We
121 do not use the MPI-GE model that was included in the past LET studies because its Southern
122 Ocean pCO₂ seasonality and decadal variability appear to be anomalously large (Gloege et al.,
123 2021; Fay and McKinley, 2021; Bennington et al., 2022a). Each individual Earth System Model
124 (ESM) is an imperfect representation of the actual Earth system, so the multiple Large Ensembles
125 are used to span different model structures and their representation of internal variability. Each
126 ensemble member undergoes the same external forcing (i.e., historical atmospheric CO₂ before
127 2005 and Representative Concentration Pathway 8.5 through 2016, plus solar and volcanic
128 forcing), but the spread across the ensemble members gives a unique trajectory of the ocean-
129 atmosphere state over time, i.e., a different state of internal variability as well as the difference
130 across models.

131 The LET used in this study includes monthly 1°x1° model output from 1982-2016 (Gloege
132 et al., 2021). For each individual ensemble member of the LET, surface ocean pCO₂ and co-located
133 driver variables (i.e., SST, SSS, Chl-a, MLD, xCO₂) were sampled monthly at a 1°x1° resolution,
134 at times and locations equivalent to SOCAT and Saildrone USV observations (**Fig. 1**; Step 1).
135 While the SOCAT observations were sampled from the testbed matching the actual years of
136 sampling, the USV observations were sampled from the testbed starting in 2007 (for ten-year
137 sampling) or 2012 (for five-year sampling) (see **Sect. 2.4**). As our focus is on reconstruction for
138 the open ocean, testbed output for coastal areas, the Arctic Ocean (>79°N) and marginal seas
139 (Hudson Bay, Caspian Sea, Black Sea, Mediterranean Sea, Baltic Sea, Java Sea, Red Sea and Sea
140 of Okhotsk) were removed prior to algorithm processing.

141



142 **Figure 1:** Schematic of the Large Ensemble Testbed (LET; modified from Gloege et al., 2021). **1:** Surface ocean
 143 pCO₂ from each of the 75 model members is sampled in space and time mimicking real-world SOCAT and Saildrone
 144 USV observations (see **Fig. 2; Table 1; Section 2.5**). Prior to algorithm processing, pCO₂-Residual is calculated
 145 (**Section 2.2**). **2:** The pCO₂-Residual (target variable) and co-located driver variables (i.e., SST, SSS, MLD, Chl,
 146 xCO₂) sampled from the testbed are processed by the XGBoost (XGB) algorithm (**Section 2.3**). **3:** Based on the full-
 147 coverage of driver variables, pCO₂-Residual is reconstructed globally. This process is repeated 75 times, individually
 148 for every single testbed model member. The temperature component (pCO₂-T) is then added back to the pCO₂-
 149 Residual for each value. **4:** The globally reconstructed pCO₂ is evaluated against the ‘model truth’ at all 1°x1° grid
 150 cells. SST = sea surface temperature. SSS = sea surface salinity. MLD = mixed layer depth. Chl = chlorophyll. xCO₂
 151 = atmospheric concentration of CO₂.
 152

153

154 2.2 The pCO₂-Residual approach

155 We used the pCO₂-Residual approach following Bennington et al. (2022a), which removes the
 156 well-studied direct effect of temperature on pCO₂ from the LET model output before algorithm
 157 processing. Temperature has both direct and indirect effects on surface ocean pCO₂. The direct
 158 effect of temperature, due to solubility and chemical equilibrium, is that an increase in temperature
 159 directly causes an increase in pCO₂ (Takahashi et al., 1993). Indirectly, temperature changes are
 160 associated with biological production and wintertime vertical mixing; and these processes tend to
 161 result in opposing pCO₂ changes. To build reconstruction algorithms through the data-driven
 162 training that occurs in ML, the statistics in all other algorithms developed to date must identify a
 163 function that disentangles these competing effects of SST on pCO₂. Here, the algorithm is assisted
 164 by removing this known temperature effect, and it must therefore only learn the pCO₂ impacts

165 from biogeochemical drivers. The pCO₂-Residual method leads to physically understandable
166 connections between the input data and output (Bennington et al., 2022a), which mitigates to some
167 degree ‘black box’ concerns typically associated with ML algorithms (Toms et al., 2020). Further,
168 this method has been shown to perform better against independent observations than other
169 common mapping methods (Bennington et al., 2022a). A brief description is provided here, but
170 for further details see Bennington et al. (2022a).

171 The temperature-driven component of pCO₂ (pCO₂-T) is calculated using this equation:

$$172 \quad p\text{CO}_2\text{-T} = p\text{CO}_2^{\text{mean}} * \exp[0.0423 * (\text{SST} - \text{SST}^{\text{mean}})]$$

173 where pCO₂^{mean} and SST^{mean} is the long-term mean of surface ocean pCO₂ and temperature,
174 respectively, using all 1°x1° grid cells from the testbed. Once pCO₂-T is determined, pCO₂-
175 Residual is calculated as the difference between pCO₂ and the calculated pCO₂-T:

$$176 \quad p\text{CO}_2\text{-Residual} = p\text{CO}_2 - p\text{CO}_2\text{-T}$$

177 Prior to algorithm processing, pCO₂-Residual values > 250 μatm and < -250 μatm from the
178 testbed were filtered out targeting values that are not representative of the real ocean. The majority
179 of the pCO₂-Residual values that were filtered out correspond to high pCO₂, above the maximum
180 value in SOCAT (816 μatm; Stamen et al., 2020). The excluded data points (less than 0.2 % per
181 member) mostly occurred in output from the CanESM2 model, and were restricted geographically,
182 predominantly along the western coastline of South America.

183 The eXtreme Gradient Boosting method (XGB; Chen and Guestrin, 2016) is used to
184 develop an algorithm that allows driver variables (i.e., SST, SSS, Chl-a, MLD, xCO₂) to predict
185 the pCO₂-Residual (**Fig. 1**; Step 2). The pCO₂-Residual and associated feature variables is split
186 into validation, training and testing sets. The test and validation set each account for 20 % of the
187 data, leaving 60 % for training. The validation set is used to optimize the algorithm
188 hyperparameters, which define the architecture of decision trees used in the model. The training
189 set is used to build the decision trees in XGB, while the test set is used to evaluate the performance
190 of the final algorithm. The XGB algorithm for this study used 4,000 decision trees with a maximum
191 depth of 6 levels, and this was fixed for all experiments. For the final reconstruction of surface

192 ocean pCO₂ across all space and time points, the previously calculated pCO₂-T values are added
193 back to the reconstructed pCO₂-Residual (**Fig. 1**; Step 3).

194 The full XGB process, including 1) training/evaluating/testing and 2) reconstructing
195 globally at a monthly resolution, was repeated individually for each LET member. This process
196 provided therefore a total of 75 unique reconstruction vs. ‘model truth’ pairs, which can be
197 statistically compared (**Fig. 1**; Step 4).

198 *2.3 Statistical Analysis in the Testbed*

199 The statistical comparisons between the test set and the reconstructions are equivalent to what
200 would be derived using real-world data (‘seen’ values). Here, we calculate error statistics based on
201 the full reconstruction (pCO₂ from all 1°x1° grid cells of the testbed, except for those masked or
202 filtered out). In the full reconstruction, ~ 99 % of the data do not correspond to SOCAT or
203 Saildrone USV observations used to train the algorithm (**Fig. S1**). Training data would ideally be
204 removed before performance evaluation, but since the training data represent only ~ 1 %, the
205 impact of not removing them is negligible (**Fig. S2**). A suite of statistical metrics can be used to
206 compare the reconstruction to the ‘model truth’ in order to assess how well the algorithm can
207 extrapolate from sparse data to full-field coverage (**Fig. 1**; Step 4). In this study, we focus on bias
208 and root-mean-squared error (RMSE). Bias is calculated as ‘mean prediction – mean observation’
209 (i.e., pCO₂ predicted by XGB subtracted by the pCO₂ ‘model truth’), and is a measure of over- or
210 underestimation in the reconstructions. RMSE measures the magnitude of the predicted error and
211 is calculated as the square root of the mean of the squared errors. We focus our discussion on the
212 mean across 75 members of the testbed for bias and RMSE. The spread across testbed ensemble
213 members is non-negligible and will be the focus of future work; here, we present the testbed spread
214 primarily in the **Supplement**.

215 *2.4 Overview of sampling patterns and model runs*

216 First, we sampled target and driver variables from the LET based on sampling distributions
217 equivalent to that of the SOCAT database (‘SOCAT-baseline’). Then, we combined the ‘SOCAT-
218 baseline’ with testbed output representing additional Saildrone USV coverage in the Southern
219 Ocean. The additional Southern Ocean coverage was based on 1) the Sutton et al. (2021) sampling
220 campaign from 2019 (‘one-latitude’ track) and 2) realistic potential future meridional USV

221 observations ('zigzag' track) (see **Section 2.4.2; Fig. 2**). We performed a total of 10 experimental
222 runs (**Table 1**). These represent different sampling approaches, including: 1) repeating USV
223 sampling over a five- or ten-year period, 2) varying the number of USVs and thus the total number
224 of monthly $1^\circ \times 1^\circ$ observations, and 3) restricting all observations to southern hemisphere winter
225 months. By comparing the different runs, we can assess whether or not certain targeted sampling
226 strategies in the Southern Ocean can improve surface ocean $p\text{CO}_2$ ML reconstructions. As
227 discussed above, the LET runs to 2016 only (Gloege et al., 2021). Saildrone USV observations
228 were therefore sampled from the testbed starting in year 2006 or 2007 (for the ten-year sampling)
229 or 2012 (for the five-year sampling) until 2016, i.e., the final year of the testbed.

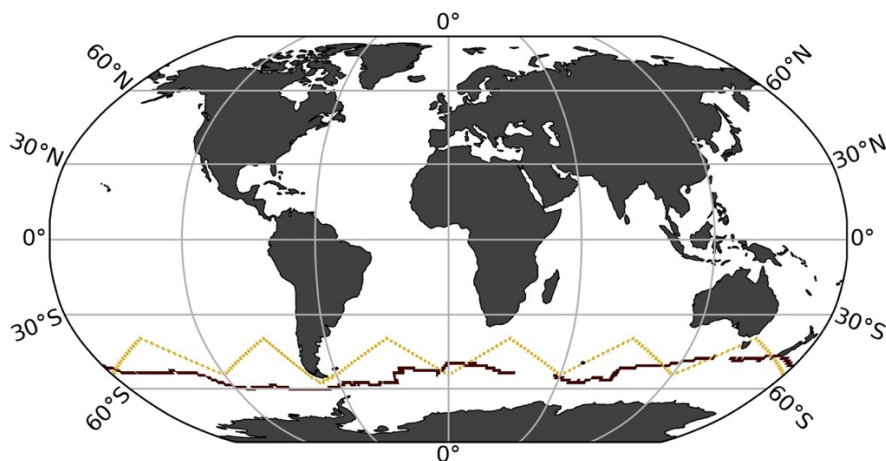
230 2.4.1 'One-latitude' runs

231 Six out of the ten experimental runs include the 'one-latitude' track (**Table 1**). The 2019 Saildrone
232 USV journey (Sutton et al., 2021) covered an 8-month period, from January to August. Since the
233 USV was recovered in early August, it did not cover the entire southern hemisphere winter (**Fig.**
234 **S3**). We repeated this 'one-latitude' eight-month sampling pattern for five years ('5Y_J-A'; 2,075
235 observations) and ten years ('10Y_J-A'; 4,150 observations). To evaluate year-round ('YR')
236 coverage, the eight-month sampling period (January-August) was shifted by one month each year
237 for ten years ('10Y_YR'; 4,150 observations). To evaluate the impact of increased sampling, the
238 2019 Saildrone USV track was repeated 12 times with incremental offsets of 1° from the original
239 track, covering an additional 6° north and south (**Fig. S4**). This 'high-sampling'-run ('x13_10Y_J-
240 A'; 44,250 observations) represents a total of 13 USVs. We also performed an additional 13 USV
241 run, but including observations from southern hemisphere winter ('W') months only
242 ('x13_10Y_W'; 25,395 observations). Finally, considering the cost of deploying 13 USVs, a
243 downscaled 'multiple-USV-winter-only'-run was tested, including five USVs sampling over a
244 period of five years ('x5_5Y_W'; 5,022 observations). This run covers an additional 2° north and
245 south from the original USV track.

246 2.4.2 'Zigzag' runs

247 Four of the ten experimental runs represent realistic potential meridional sampling in the Southern
248 Ocean ('zigzag' tracks; **Table 1**) as suggested by Djeutchouang et al. (2022). Saildrone USVs can
249 operate at a speed capable of covering the spatial extent of meridional gradients in the Southern

250 Ocean (Djeutchouang et al., 2022). However, Saildrone USVs are solar powered, and thus their
251 range is restricted by the availability of solar radiation. To account for this and maintain a realistic
252 sampling scenario, sampling occurs only to a maximum latitude of 55° S in these experiments.
253 This alternative sampling pattern represents USVs sailing west to east in a north/south ‘zigzag’
254 pattern covering 40° S and 55° S for every 30° of longitude (**Fig. 2**). We created two scenarios.
255 For the first scenario, every 30° of longitude from 40° S and 55° S is visited every three months
256 within a single year as suggested by Lenton et al. (2006). Assuming an average Saildrone USV
257 speed, this scenario represents four platforms equally spaced around the Southern Ocean. This
258 sampling pattern was repeated for 10 years, with year-round coverage (‘Zx4_10Y_YR’; 7,600
259 observations), and for southern hemisphere winter months only (‘Zx4_10Y_W’; 2,500
260 observations). The second scenario represents a ‘high-sampling’ strategy, where every 30° of
261 longitude from 40° S and 55° S is visited approximately monthly. This can be achieved by
262 deploying 10 platforms equally spaced around the Southern Ocean running at an average Saildrone
263 USV speed. This sampling pattern is repeated for five years, sampling year-round
264 (‘Z_x10_5Y_YR’; 11,400 observations) and during southern hemisphere winter months only
265 (‘Z_x10_5Y_W’; 3,800 observations).



266
267 **Figure 2:** Saildrone Uncrewed Surface Vehicle (USV) tracks representing the first circumnavigation around
268 Antarctica from 2019 in maroon (‘one-latitude’ track; Sutton et al., 2021) and an alternative virtual route with
269 meridional coverage (‘zigzag’ track).

Run name	SOCAT-baseline	5Y J-A	10Y J-A	10Y YR	x13 10Y J-A	x13 10Y W	x5 5Y W	Z x4 10Y YR	Z x4 10Y W	Z x10 5Y YR	Z x10 5Y W
Saildrone track	NA	One-lat	One-lat	One-lat	One-lat	One-lat	One-lat	Zigzag	Zigzag	Zigzag	Zigzag
Years of sampling	NA	5	10	10	10	10	5	10	10	5	5
Duration of sampling	NA	Jan-Aug	Jan-Aug	Year-round	Jan-Aug	SO winter	SO winter	Year-round	SO winter	Year-round	SO winter
Additional observations	NA	2,075	4,150	4,150	44,250	25,395	5,022	7,600	2,500	11,400	3,800
Global coverage increase (%)	NA	0.01	0.02	0.02	0.3	0.1	0.03	0.04	0.01	0.07	0.02
Mean bias (μatm)											
<i>Testbed period (1982-2016)</i>											
Globally	0.63	0.59	0.59	0.52	0.53	0.39	0.57	0.51	0.51	0.45	0.44
NORTH (35°N-90°N)	0.11	0.24	0.20	0.25	0.20	0.17	0.16	0.16	0.16	0.12	0.20
MID (35°S-35°N)	0.23	0.21	0.22	0.14	0.20	0.15	0.23	0.20	0.18	0.13	0.18
SOUTH (90°S-35°S)	1.4	1.3	1.2	1.1	1.1	0.80	1.2	1.1	1.1	1.0	0.87
SO winter months (JJA)	1.3	1.2	1.2	1.1	1.1	0.90	1.2	0.93	1.0	0.94	0.95
SO summer months (DJF)	0.070	0.11	0.15	0.10	0.15	0.019	0.11	0.25	0.073	0.16	0.066
<i>2006/2012-2016</i>											
Globally	0.51*	0.27	0.34	0.28	0.19	0.03	0.21	0.23	0.24	0.17	0.07
SOUTH (90°S-35°S)	1.6*	0.93	1.1	1.0	0.72	0.37	0.73	0.89	0.92	0.67	0.55
SOUTH (90°S-35°S) Jun, Jul, Aug	4.2*	2.6	2.7	2.8	2.2	1.8	2.5	1.8	2.4	1.2	2.0
Mean RMSE (μatm)											
<i>Testbed period (1982-2016)</i>											
Globally	11.8	11.7	11.8	11.7	11.7	11.6	11.7	11.5	11.6	11.5	11.6
NORTH (35°N-90°N)	13.0	13.0	13.0	13.0	13.0	13.0	13.1	13.0	13.0	13.0	13.0
MID (35°S-35°N)	11.7	11.7	11.7	11.7	11.7	11.7	11.7	11.7	11.7	11.7	11.7
SOUTH (90°S-35°S)	11.5	11.3	11.4	11.2	11.1	11.0	11.3	11.0	10.7	10.6	11.0
<i>2006/2012-2016</i>											
Globally	11.6*	11.6	11.4	11.3	11.3	11.2	11.6	11.0	11.2	11.1	11.4
SOUTH (90°S-35°S)	11.4*	11.1	11.0	10.7	10.6	10.4	10.9	10.0	10.6	9.7	10.6
SOUTH (90°S-35°S) Jun, Jul, Aug	12.0*	11.3	11.2	10.9	10.5	10.3	11.1	10.3	10.6	9.6	10.3

270
271 **Table 1.** Overview of the different sampling experiments tested in this study, and mean bias and RMSE (in μatm) for
272 various time periods, latitude bands for all runs. Bold values represent the best score for each category. ‘One-lat’ =
273 ‘one-latitude’ track; incorporates the Saildrone USV route from Sutton et al. (2021). ‘Zigzag’ = potential meridional
274 sampling. ‘Additional observations = number of $1^\circ \times 1^\circ$ monthly Saildrone USV observations in addition to SOCAT.
275 J-A= January-August. YR = year-round. W = southern hemisphere winter. x4, x5, x10 and x13 = four, five, ten and
276 13 USVs. SO winter = Southern Ocean winter months, i.e., June, July, August and also including September. *Average
277 value of the mean of 2006-2016 and 2012-2016. The global coverage increase was calculated based on the total
278 number of available 1982-2016 monthly $1^\circ \times 1^\circ$ observations from SOCAT (262,204 observations) and the Large
279 Ensemble Testbed (17,290,470 observations).

280
281 **2.5 Air-sea CO_2 flux**

282 To assess the global ocean carbon sink associated with our pCO_2 reconstructions, air-sea CO_2
283 exchange was calculated for 1985 onward. Here, we computed air-sea CO_2 fluxes using the bulk
284 formulation with python package Seaflux.1.3.1 (<https://github.com/lukegre/SeaFlux>; Gregor et al.
285 2021; Fay et al., 2021). We calculated global and Southern Ocean flux in the same manner for 1)
286 the testbed ‘model truth’, 2) the ‘SOCAT-baseline’ and 3) the 10 experimental USV runs.

287 The net sea–air CO_2 flux was estimated using:

288
$$\text{Flux} = k_w \cdot \text{sol} \cdot (\text{pCO}_2^{\text{ocn}} - \text{pCO}_2^{\text{atm}}) \cdot (1 - \text{ice})$$

289 where ‘ k_w ’ is the gas transfer velocity, ‘sol’ is the solubility of CO_2 in seawater (in units of mol
290 $\text{m}^{-3} \mu\text{atm}^{-1}$), ‘ $\text{pCO}_2^{\text{ocn}}$ ’ is the partial pressure of surface ocean carbon (in μatm), either from the
291 ‘model truth’ or from the reconstructions, and $\text{pCO}_2^{\text{atm}}$ (in μatm) is the partial pressure of
292 atmospheric CO_2 in the marine boundary layer. For GFDL, we used direct model output of
293 $\text{pCO}_2^{\text{atm}}$, while for CESM and CanESM2, $\text{pCO}_2^{\text{atm}}$ was calculated individually, as the product of

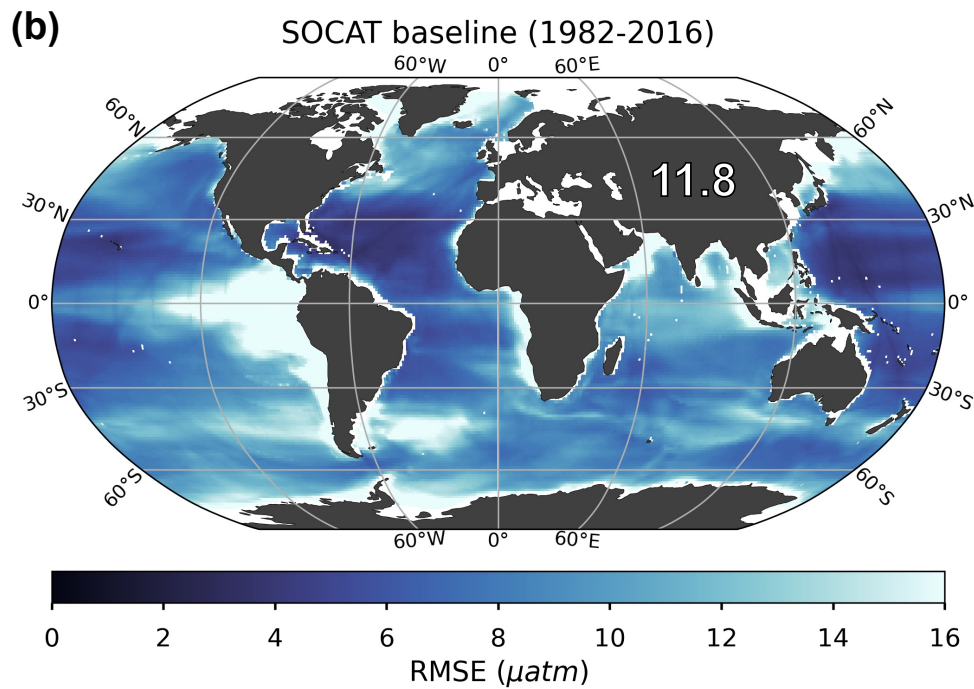
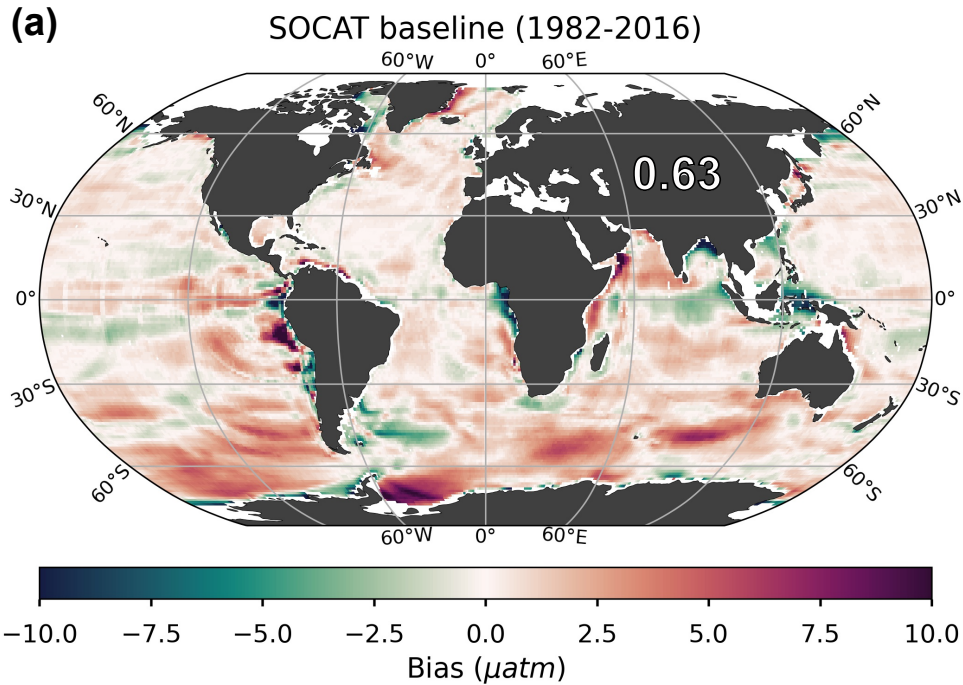
294 surface $x\text{CO}_2$ and sea level pressure (the contribution of water vapor pressure was corrected for in
295 CESM and GFDL). Finally, to account for the seasonal ice cover in high latitudes, the fluxes were
296 weighted by 1 minus the ice fraction ('ice'), i.e., the open ocean fraction. Inputs to the calculation
297 include EN4.2.2 salinity (Good et al., 2013), SST and ice fraction from NOAA Optimum
298 Interpolation Sea Surface Temperature V2 (OISSTv2) (Reynolds et al., 2002), and surface winds
299 and associated wind scaling factor from the European Centre for Medium-Range Weather
300 Forecasts (ECMWF ERA5 sea level pressure (Hersbach et al., 2020). Results presented show the
301 global and Southern Ocean ($< 35^\circ \text{S}$) fluxes in units of Pg C yr^{-1} .

302 Note that, reconstructions of pCO_2 for the 'SOCAT-baseline' and the experimental USV
303 runs are limited in their spatial extent to the open ocean (see **Sect. 2.1**; excluding coastal areas, the
304 Arctic Ocean and marginal seas). The same mask was thus also applied when calculating the flux
305 of the 'model truth', prior to comparison with the reconstructions.

306 **3. Results**

307 *3.1 Performance metrics for the 'SOCAT-baseline' reconstruction*

308 The mean bias for the entire testbed period (i.e., 1982-2016) is $0.63 \mu\text{atm}$ globally (**Fig. 3a**) and
309 $1.4 \mu\text{atm}$ for the Southern Ocean ($< 35^\circ \text{S}$; **Table 1**). Bias is much closer to zero for the mid-
310 latitudes (between 35°S and 35°N ; $0.23 \mu\text{atm}$) and northern latitudes ($> 35^\circ \text{N}$; $0.11 \mu\text{atm}$) (**Fig.**
311 **3a**). There is a significant difference in bias considering southern hemisphere winter months (June,
312 July, August) versus summer months (December, January, February), with a global mean bias (for
313 1982-2016) of $1.3 \mu\text{atm}$ compared to $0.07 \mu\text{atm}$, respectively (**Table 1**), due to the sparseness of
314 SOCAT observations from the southern hemisphere during the harsh winter season (**Fig. S5a**).
315 The mean RMSE for the entire testbed period (i.e., 1982-2016) is $11.8 \mu\text{atm}$ globally (**Fig. 3b**) and
316 $11.5 \mu\text{atm}$ for the Southern Ocean (**Table 1**). RMSE is highest in the Eastern Tropical and
317 Southeastern Pacific Ocean and in the Southern Ocean, where the algorithm generally
318 overestimates pCO_2 (i.e., positive bias; **Fig. 3a**), with some exceptions in the Atlantic section. This
319 is consistent with the areas significantly undersampled by SOCAT (**Fig. S5b**). Except for these
320 areas, RMSE and bias is generally low (close to zero) in the open ocean, but show higher values
321 along coastlines (**Fig. 3b**).



322

323 **Figure 3:** Bias **(a)** and root-mean-squared error (RMSE) **(b)** for the ‘SOCAT-baseline’ (i.e., no USV) over the period
 324 of 1982 through 2016. The global mean bias and RMSE is 0.63 μatm and 11.8 μatm , respectively. Note that only the
 325 open ocean was considered in the reconstruction, so several areas were masked out prior to algorithm processing, such
 326 as the Arctic Ocean, coastal areas and marginal seas (no data; white areas in figures).

327

328

329 3.2 Reconstruction improvements with Saildrone USV additions

330 Our presentation of global maps is limited to runs ‘x5_5Y_W’ (5,022 monthly 1°x1° observations)
331 and ‘Z_x4_10Y_YR’ (7,600 monthly 1°x1° observations). These runs were selected as they
332 represent observational schemes that are realistic in the near-term future considering logistics and
333 cost level, both non-meridional and meridional sampling, and different approaches to observing
334 duration and seasonal coverage. For the remaining runs, equivalent maps can be found in the
335 **Supplement**.

336 3.2.1 Bias

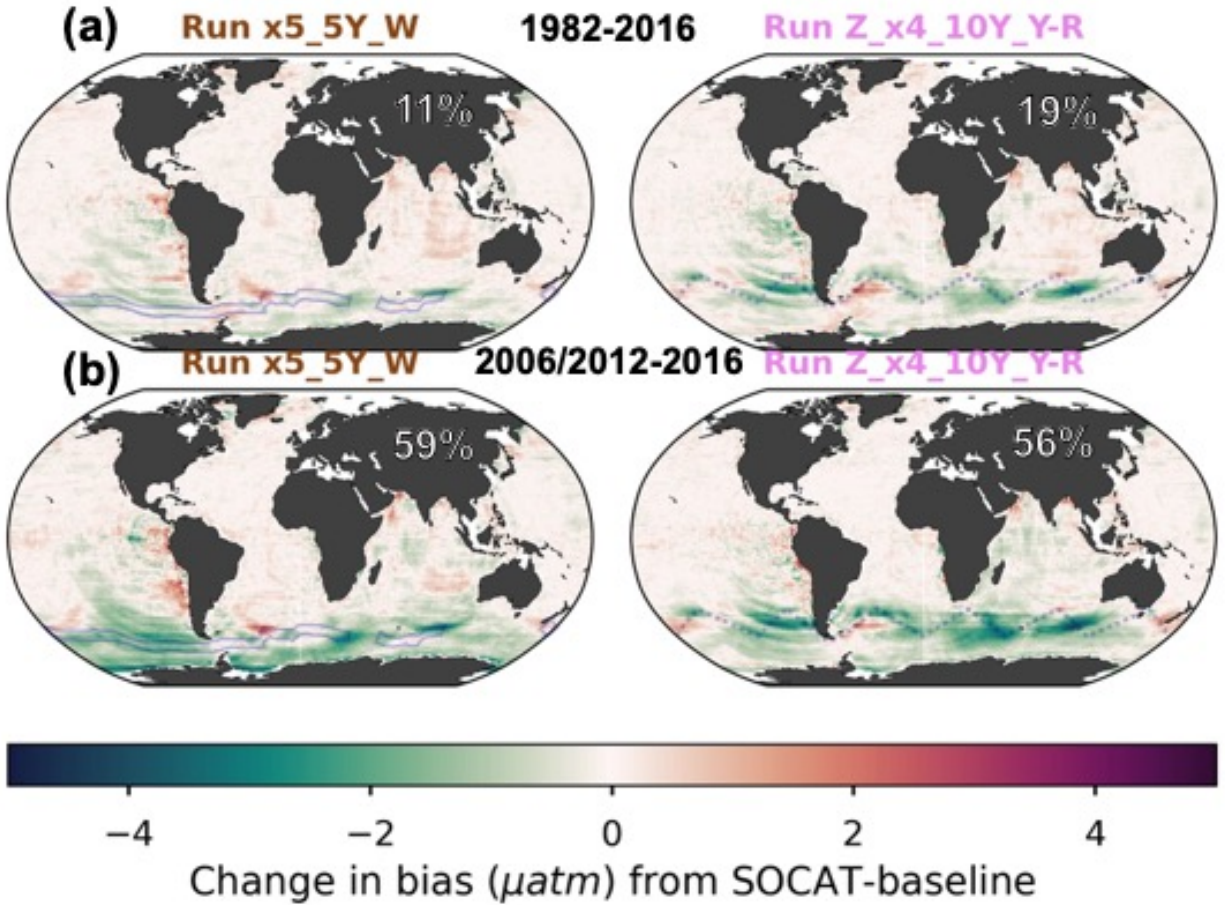
337 All Saildrone USV runs show a reduction in bias compared to the global mean 1982-2016
338 ‘SOCAT-baseline’ (**Figs. 4a, S6**). The improvement in bias is mainly due to lower reconstructed
339 pCO₂ values at southern latitudes, where the ‘SOCAT-baseline’ reconstruction generally
340 overestimates pCO₂ (**Fig. 3a**). The global mean bias for ‘zigzag’ run ‘Z_x4_10Y_YR’ is 0.51
341 µatm, a higher improvement (19 %) over the ‘SOCAT-baseline’ compared to the ‘one-latitude’
342 run ‘x5_5Y_W’ (11 % mean improvement; mean bias = 0.57 µatm;) (**Fig. 4a; Table 1**). Generally,
343 the ‘zigzag’ runs show higher improvements from the ‘SOCAT-baseline’ (19-31 % improvement;
344 resulting mean bias = 0.44-0.51 µatm) compared to the ‘one-latitude’ runs (7-19 % improvement;
345 resulting mean bias = 0.52-0.59 µatm) (**Fig. S6; Table 1**). However, the ‘one-latitude’-run
346 ‘x13_10Y_W’ that samples southern hemisphere winter months only, stands out with the lowest
347 global mean bias of 0.39 µatm, representing a 39 % mean improvement from the ‘SOCAT-
348 baseline’, as well as reduced spread across the 75 ensemble members (**Table 1; Fig. S6; S8**). This
349 run, however, has three or five times more observations (25,395) than ‘Z_x4_10Y_YR’ and
350 ‘x5_5Y_W’, respectively.

351 Compared to the entire testbed period, even larger improvements in global mean bias are
352 shown for the period of Saildrone USV additions (2006-2016 and 2012-2016; **Figs. 4a vs. 4b,**
353 **Figs. S6 vs. S7**). Compared to the ‘SOCAT-baseline’, run ‘x13_10Y_W’ results in a mean bias
354 improvement of 95 %, while the remaining ‘one-latitude’ runs and the ‘zigzag’ runs show mean
355 improvements up to 63 % and 85 %, respectively (**Fig. S7**).

356 Perhaps surprisingly, there is not a strong connection between the global or Southern Ocean
357 mean bias and the number of added USV observations (**Fig. 5**). The ‘one-latitude’ ‘high-sampling’

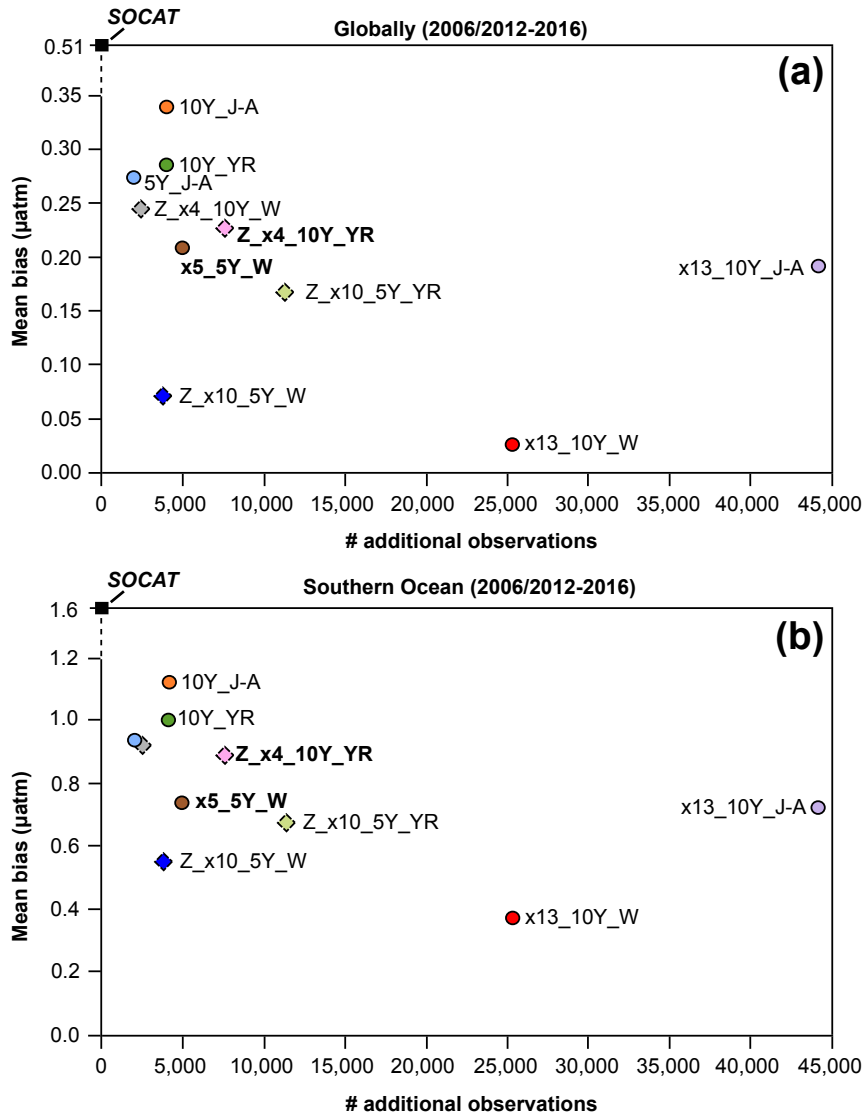
358 run ‘x13_10Y_J-A’ (44,250 observations) show similar mean bias or is outperformed by all
359 ‘zigzag’ runs as well as the ‘one-latitude’-runs that restrict sampling to southern hemisphere winter
360 months (i.e., ‘x5_5Y_W’ and ‘x13_10Y_W’).

361 Considering the change in bias from year-to-year, the ‘SOCAT-baseline’ shows positive
362 bias at all latitudes in the beginning of the testbed period, before improvement occurs around 1990
363 (**Fig. 6a**). This is consistent with increasing SOCAT sampling with time for the period considered
364 here (i.e., up to 2016; **Fig. S5c**). As SOCAT observations are biased towards the northern
365 hemisphere (**Fig. S5a, b**), bias in the Southern Ocean ($< 35^\circ$ S) increases significantly starting in
366 the 2000s and remains high until the end of the testbed period (**Fig. 6a**). By adding USV sampling,
367 bias in the Southern Ocean improves over the ‘SOCAT-baseline’ around year 2000 (**Fig. 6b-d**;
368 **Fig. S9**), up to 6-12 years before to the introduction of additional samples in either 2006 or 2012.
369 This improvement is shown for the majority of the 75 ensemble members (**Fig. S10**). Run
370 ‘Z_x10_5Y_W’, which has the lowest mean bias out of the ‘zigzag’ runs (**Fig. 5**), shows
371 improvement even further back in time, until the beginning of the testbed period (**Fig. S9**). While
372 the annual mean bias of the ‘zigzag’ runs varies rather consistently, there is a larger spread across
373 the ‘one-latitude’ runs (**Fig. 6d**).

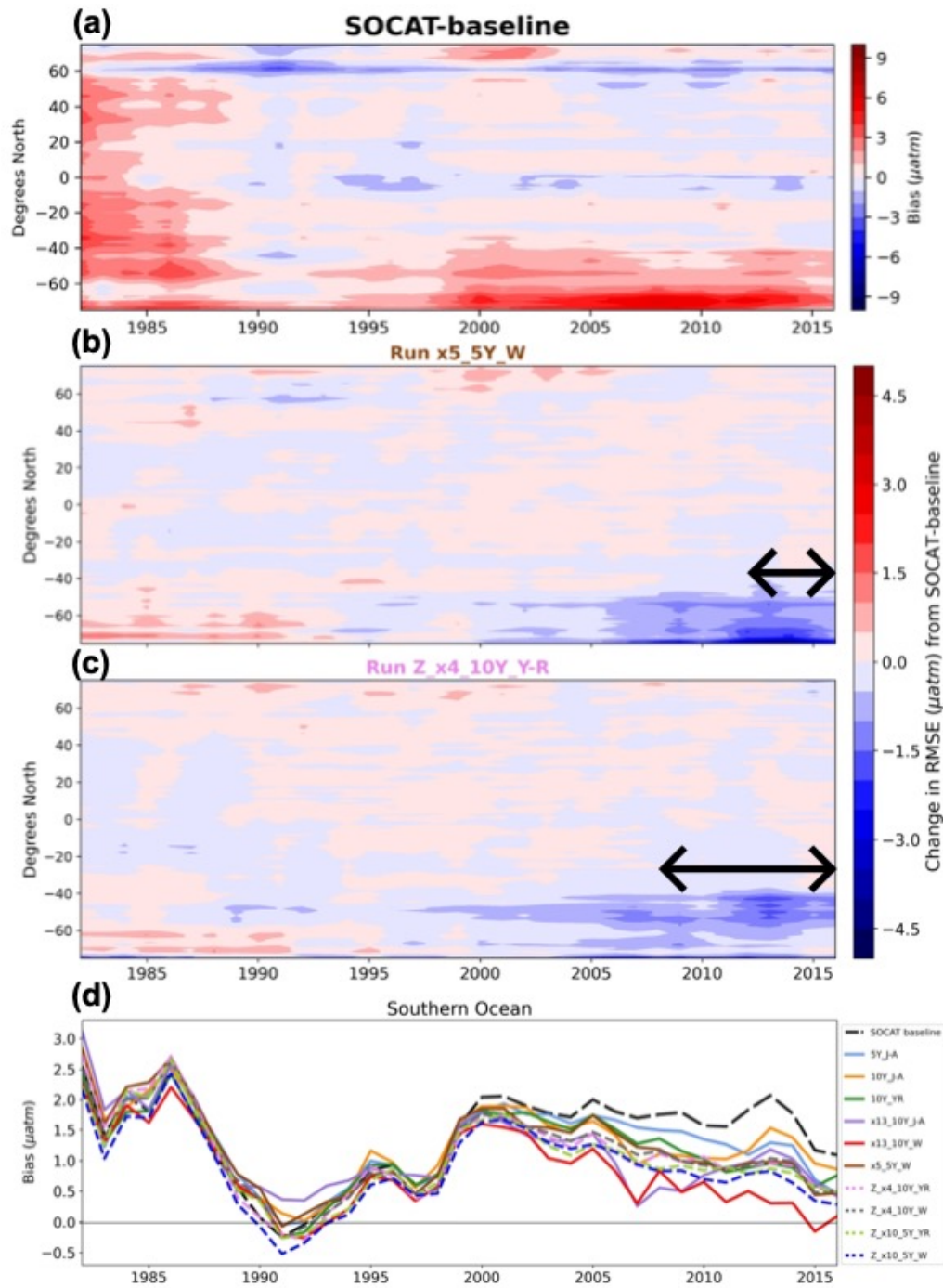


374
 375
 376
 377
 378

Figure 4: Change in bias when comparing run ‘x5_5Y_W’ and ‘Z_x4_10Y_YR’ to the ‘SOCAT-baseline’ reconstruction, averaged over the duration of the testbed period (a; 1982-2016) and the period of USV additions (b; 2006-2012 or 2012-2016). The percent global improvement in absolute bias is shown on each panel.



379
 380 **Figure 5:** Mean bias globally (a) and for the Southern Ocean (b) for the duration of Saildrone USV sampling (2006-
 381 2016 or 2012-2016) for all runs presented in **Table 1**. Circles represent runs using the ‘one-latitude’ track, while
 382 diamonds represent ‘zigzag’ runs. Runs highlighted in bold correspond to the two selected runs mapped in **Figure 4**,
 383 **6**, **7** and **9**. Global (0.51 µatm) and Southern Ocean (1.6 µatm) bias values shown for the ‘SOCAT-baseline’ (black
 384 squares) represent a mean of values for 2006-2016 (global = 0.52 µatm, S. Ocean = 1.63 µatm) and 2012-2016 (global
 385 = 0.51 µatm, S. Ocean = 1.56 µatm). ‘# additional observations’ = number of monthly 1°x1° USV observations in
 386 addition to SOCAT. Box plots illustrating the spread across the 75 ensemble members are shown in **Fig. S8**.



388

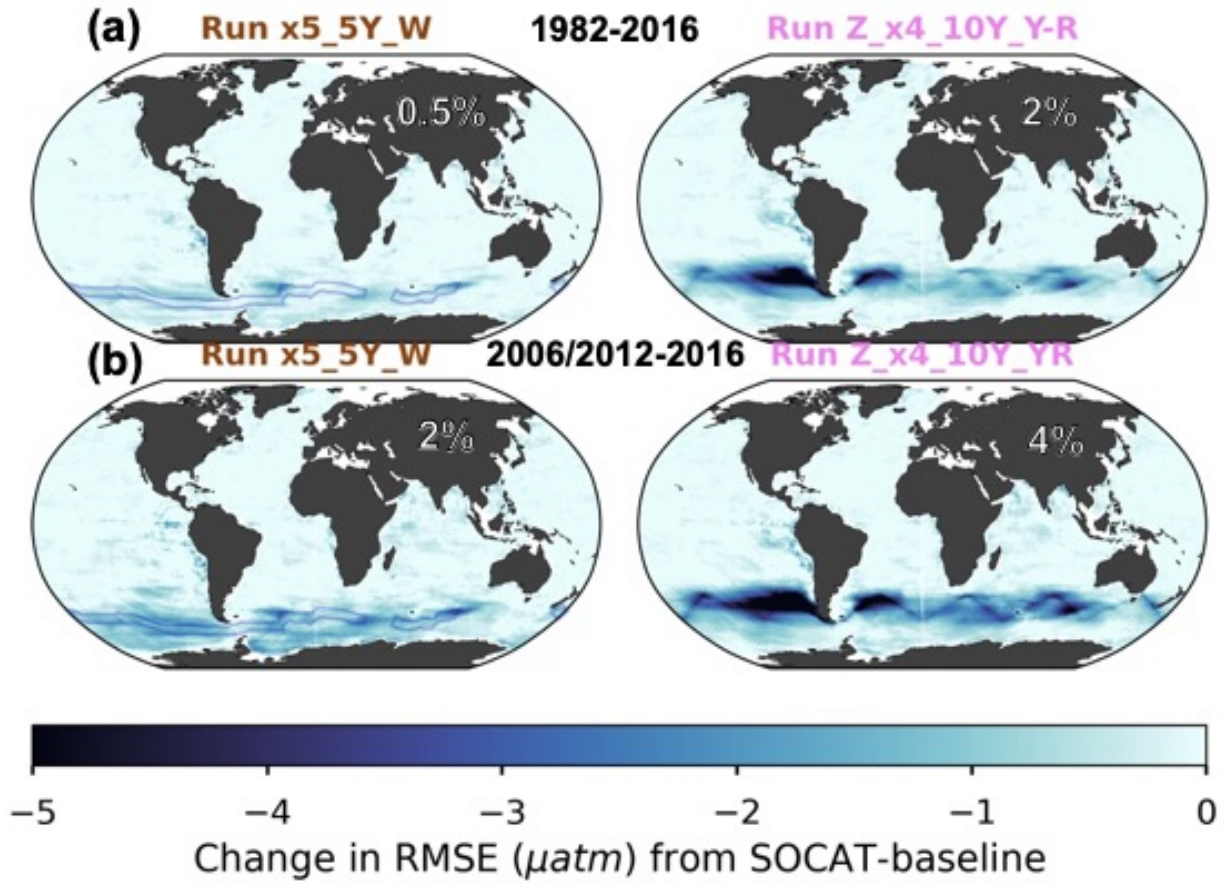
389 **Figure 6:** Zonal mean, annual mean Hovmöller of bias for the ‘SOCAT-baseline’ (a). Change in bias for run
 390 ‘x5_5Y_W’ (b) and ‘Z_x4_10Y_YR’ (c) compared to the ‘SOCAT-baseline’ shown in (a). Improvement in bias in
 391 the Southern Ocean expands back in time well beyond the duration of USV additions for both runs (shown by arrows
 392 on each panel). Annual mean bias for the Southern Ocean (> 35° S) for all runs (d).

393

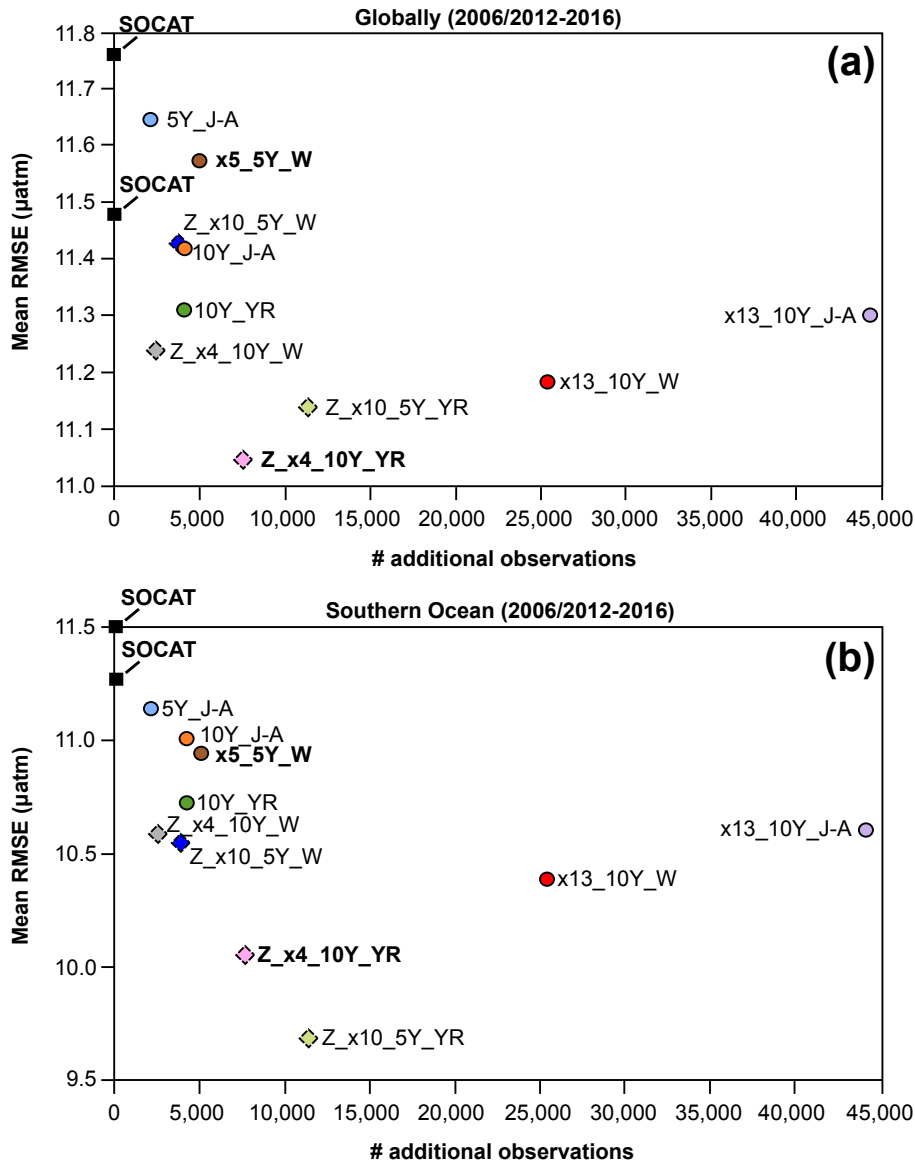
394 3.2.2 Root-mean squared error (RMSE)

395 Similar to bias, improvements in RMSE are most significant during the period of USV additions
396 and within the Southern Ocean (**Fig. 7a** vs. **7b**). For the duration of USV additions, the ‘one-
397 latitude’ runs show improvements in global mean RMSE of 1-3 % (0.1-1 % for 1982-2016), while
398 the ‘zigzag’ runs show higher improvements between 2-5 % (1-3 % for 1982-2016) (**Figs. 7, S11,**
399 **S12**). Mean RMSE is further reduced in the Southern Ocean by up to 16 %, and during southern
400 hemisphere winter months (JJA) up to 21 % (run ‘Z_x10_5Y_YR’; mean RMSE of 9.6 μatm ;
401 **Table 1**). There is minimal change in RMSE (or bias) during southern hemisphere summer months
402 (DJF; **Fig. S13**). The two ‘zigzag’ runs sampling year-round (‘Z_x4_10Y_YR’ and
403 ‘Z_x10_5Y_YR’) have the lowest RMSE values both globally and in the Southern Ocean (**Fig. 8**).
404 The spread across the 75 testbed members for each experiment is shown in **Figure S14**.

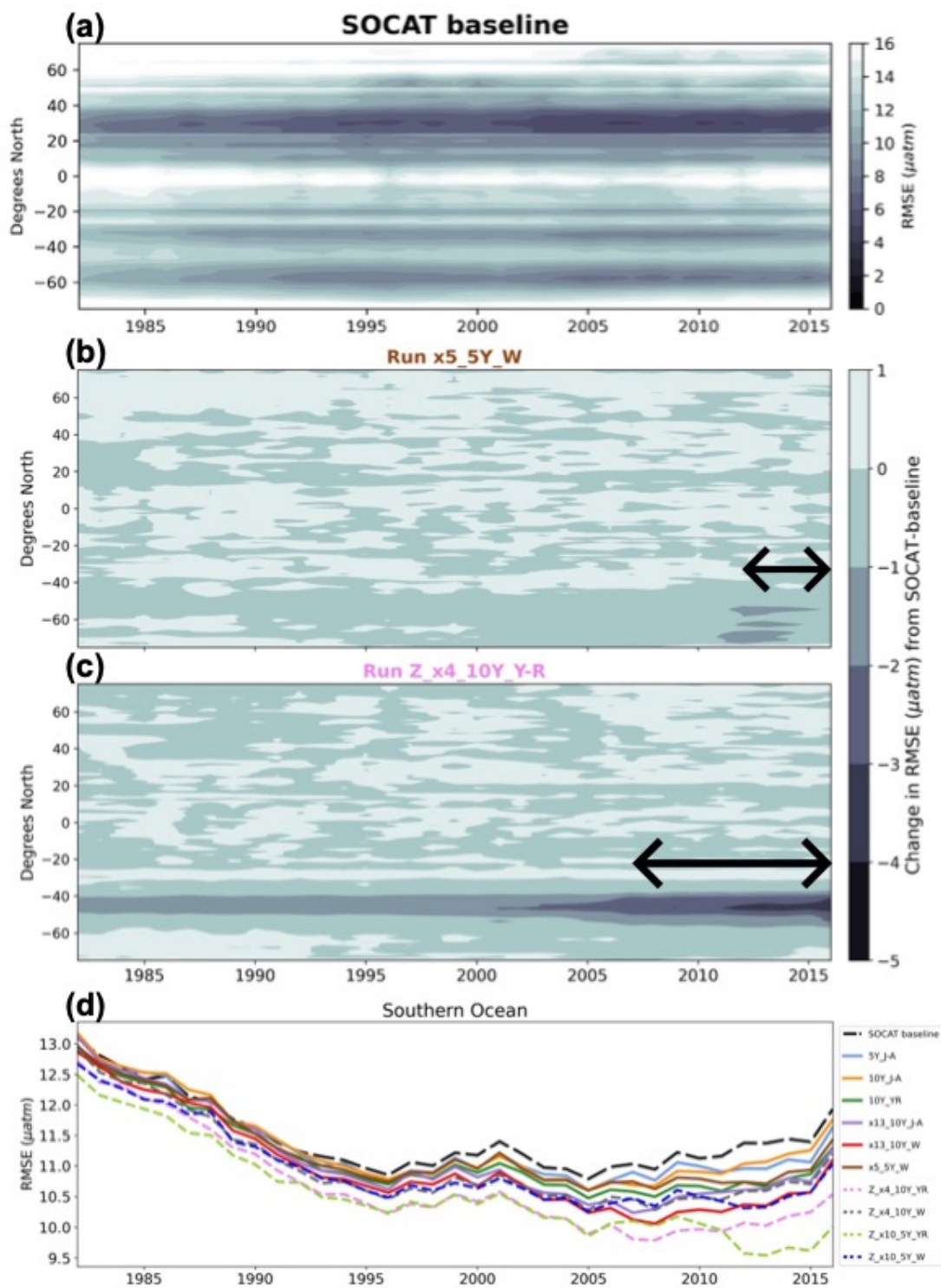
405 The ‘zigzag’ runs, as well as the ‘high-sampling’ ‘one-latitude’-runs (i.e., ‘x13_10Y_J-A’
406 and ‘x13_10Y_W’), show improvements compared to the ‘SOCAT-baseline’ from the initiation
407 of sampling (**Figs. 9, S15, S16**). The year-round ‘zigzag’ runs, however, show improvement in the
408 Southern Ocean from the beginning of the testbed period (**Figs. 9c, d, S15**). RMSE improvements
409 back in time are greater for all runs in the southern hemisphere winter months (**Fig. S17**).



410
 411 **Figure 7:** Change in RMSE when comparing run 'x5_5Y_W' and 'Z_x4_10Y_YR' to the 'SOCAT-baseline',
 412 averaged over the duration of the testbed period (a; 1982-2016) and the period of Saildrone USV additions (b; 2006-
 413 2012 or 2012-2016). The percent global improvement is shown on each panel.



414
 415 **Fig. 8:** Mean RMSE globally (a) and for the Southern Ocean (< 35° S; b) for the duration of Saildrone USV sampling
 416 (2006-2016 or 2012-2016) for all runs presented in **Table 1**. Circles represent runs using the ‘one-latitude’ track, while
 417 diamonds represent ‘zigzag’ runs. Runs highlighted in bold correspond to the two selected runs mapped in **Figure 4,**
 418 **6, 7** and **9**. RMSE values shown for the ‘SOCAT-baseline’ (black squares) represent a mean of values for 2006-2016
 419 (global = 11.5 µatm, S. Ocean = 11.3 µatm) and 2012-2016 (global = 11.8 µatm, S. Ocean = 11.5 µatm). ‘# additional
 420 observations’ = number of monthly 1°x1° USV observations in addition to SOCAT. Box plots illustrating the spread
 421 across the 75 ensemble members are shown in **Fig. S14**.



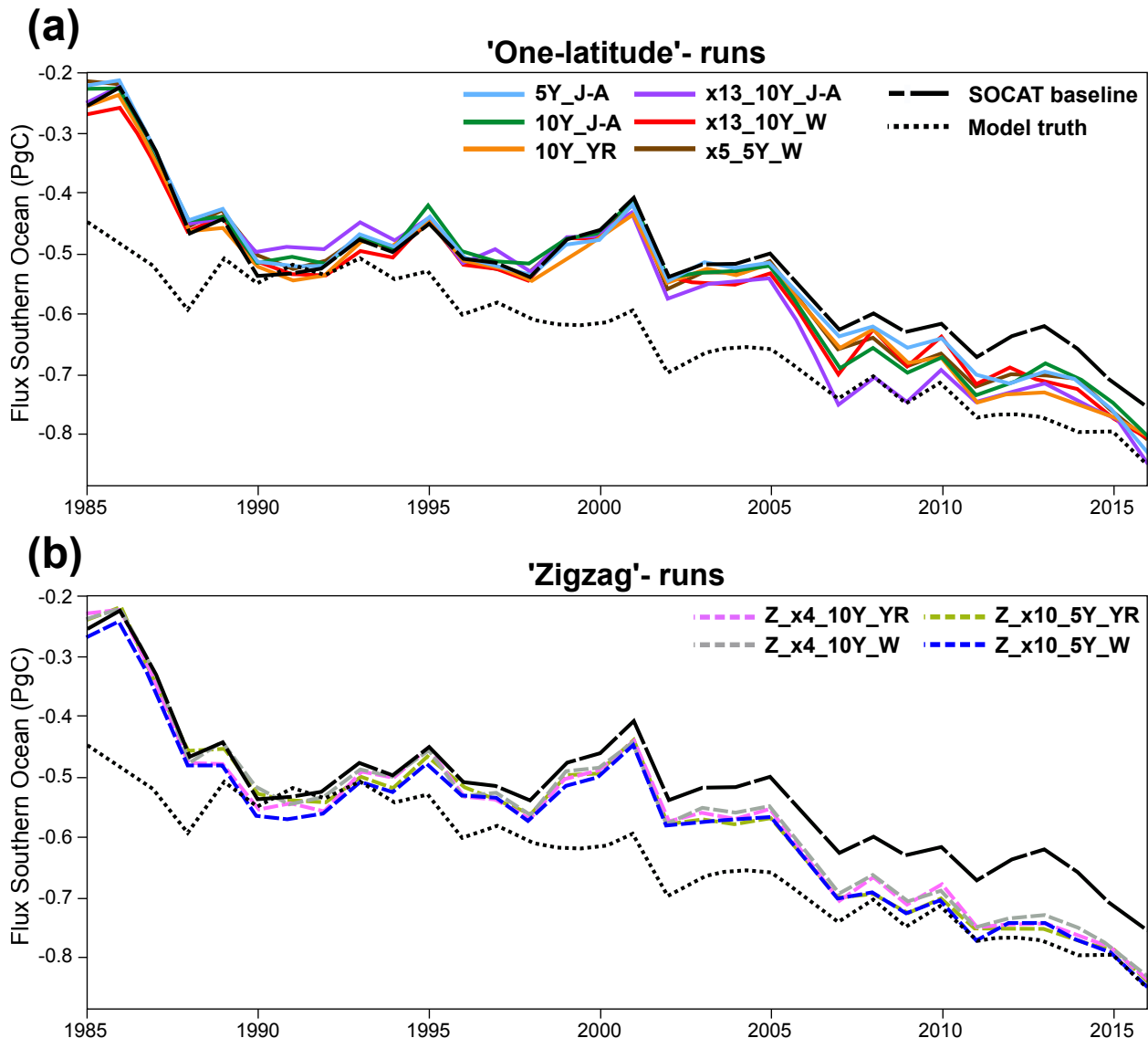
424 **Figure 9:** Zonal mean, annual mean Hovmöller of RMSE for the ‘SOCAT-baseline’ (a). Change in RMSE for run
 425 ‘x5_5Y_W’ (b) and ‘Z_x4_10Y_YR’(c) compared to the ‘SOCAT-baseline’. Run ‘Z_x4_10Y_YR’ shows
 426 improvement in RMSE within the Southern Ocean, which expand well beyond the duration of Saildrone USV
 427 additions (shown by arrow on panel). Annual mean RMSE for the Southern Ocean (> 35° S) for all runs (d).

428 *3.3 Impact on the air-sea CO₂ flux with Saildrone USV additions*

429 Air-sea flux was calculated in the same manner for both the ML reconstructions and the ‘model
430 truth’, which allows for the isolation of the impact of different sampling strategies, as mediated by
431 the pCO₂ reconstruction, on fluxes (see **Sect. 2.5**). These flux estimates are made to inform
432 understanding of the errors that may exist in CO₂ flux estimates derived from pCO₂
433 reconstructions, and how new sampling could address these errors. Flux estimates represent the
434 average of the 75 members of the LET in each case, and are not estimates of real-world fluxes.

435 Compared to the ‘model truth’, the ‘SOCAT-baseline’ reconstruction underestimates the
436 global and Southern Ocean sink by 0.11-0.13 Pg C yr⁻¹ over 1982-2016 (**Fig. 10; Table S1**).
437 Regardless of sampling pattern, adding Saildrone USV observations increases both the global and
438 Southern Ocean mean sink compared to the ‘SOCAT-baseline’ (**Figs. 10, S18**). The ‘one-latitude’
439 runs show an increase of 0.01-0.03 Pg C yr⁻¹ (2-6 % strengthening) of the Southern Ocean sink
440 (1982-2016), while the ‘zigzag’ runs lead to an even stronger sink by 0.04-0.06 Pg C yr⁻¹ (7-11 %
441 strengthening) (**Table S2**). When averaging over the years of Saildrone USV sampling addition
442 (i.e., 2006-2012 and 2012-2016), the Southern Ocean sink increases up to 0.09 Pg C yr⁻¹ (14 %
443 strengthening) for the ‘one-latitude’ runs and up to 0.1 Pg C yr⁻¹ (15 % strengthening) for the
444 ‘zigzag’ runs (**Table S2**). These same features are found for the global ocean (**Fig. S18; Table**
445 **S2**).

446 All of the ‘zigzag’ runs quite closely match both the global and Southern Ocean ‘model
447 truth’ air-sea CO₂ flux for the duration of sample additions (**Figs. 10, S18**). Except for the first
448 couple of years of sample addition for the ‘high-sampling’-run ‘x13_10Y_J-A’, none of the ‘one-
449 latitude’ runs can match the ‘model truth’ air-sea CO₂ flux, instead they all underestimate the flux
450 (**Figs. 10, S18**). The ‘zigzag’ runs have impact on the air-sea flux from an earlier date, starting to
451 pull the results away from the ‘SOCAT-baseline’ and toward the ‘model truth’ already in the late-
452 1990s, while the ‘one-latitude’ runs do the same about a decade later (**Figs. 10, S18**).



453 **Figure 10:** Southern Ocean (< 35° S) annually averaged air-sea CO₂ flux for the ‘SOCAT-baseline’ (black dashed
 454 line), ‘model truth’ (black dotted line) ‘one-latitude’ runs (a; solid lines) and ‘zigzag’ runs (b; dashed lines).
 455

456

457

458 **4. Discussion**

459 We have tested the pCO₂-Residual reconstruction method with the Large Ensemble Testbed (LET)
 460 to estimate its fidelity and understand how new samples could increase skill. We find that,
 461 regardless of the chosen Sairdrone USV sampling pattern, the reduction in mean bias and mean
 462 RMSE compared to the ‘SOCAT-baseline’ is most prominent within the Southern Ocean (< 35°
 463 S) during the period of which Sairdrone USV observations were added (Figs. 4, 6, 7, 9). However,
 464 it is important to mention that additional Southern Ocean sampling also improves pCO₂

465 reconstructions globally (**Figs. 5a, 8a**). Based on our experiments, a combination of factors
466 improve global and Southern Ocean pCO₂ reconstructions, including the type of sampling pattern
467 and seasonality of sampling, and to some extent, the number of additional observations.
468 Importantly, increasing the number of observations or duration of sampling (5 vs. 10 years) is not
469 the sole determining factor for improving the reconstructions (**Figs. 5, 8**). This is best demonstrated
470 by the ‘high-sampling’-run ‘x13_10Y_J-A’ (44,250 observations), which does not provide
471 significantly better reconstructions, or is even outperformed, by runs with 2-18 times fewer
472 observations. The runs that produce lower mean RMSE do include data throughout southern
473 hemisphere winter (**Figs. 8, 9d**). Run ‘x13_10Y_J-A’ does not include more than a few
474 observations in the month of August, as it follows the temporal pattern of the real-world ‘one-
475 latitude’ Saildrone USV expedition (**Fig. S2**; Sutton et al., 2021). The ‘one-latitude’ runs ‘10Y_J-
476 A’ and ‘10Y_YR’ are directly comparable in terms of sample duration, spatial extent and number
477 of observations (**Table 1**), but the latter, which covers all months, always shows lower mean
478 RMSE and bias (**Figs. 5, 6d, 8, 9d**). These examples attest to the importance of addressing the
479 issue of significant undersampling in the Southern Ocean during the winter season (**Figs. S5a, b**).

480 Another important comparison is the ‘one-latitude’-run ‘x5_5Y_W’ (5,022 observations)
481 and ‘zigzag’-run ‘Z_x10_5Y_W’ (3,800 observations) that both sample during southern
482 hemisphere winter months over a five-year period (**Table 1**), where the ‘zigzag’-run consistently
483 performs better even though it includes fewer observations (**Figs. 5, 8**). Most of the runs that
484 perform similar to, or outperform, the above-mentioned ‘high-sampling’-run ‘x13_10Y_J-A’
485 (44,250 observations), sample in a ‘zigzag’ pattern. Out of all 10 runs, the ‘year-round’ ‘zigzag’
486 runs (‘Z_x4_10Y_YR’ and ‘Z_x10_5Y_YR’) are most able to reduce the mean error as shown by
487 the lowest RMSE values (**Figs. 8, 9d**). A recent study performed similar sampling experiments as
488 shown here, by comparing sampling from different types of autonomous platforms to a ‘SOCAT-
489 baseline’ (Djeutchouang et al., 2022). They emphasized the importance of capturing the significant
490 differences in pCO₂ that exist across meridional gradients during summer and winter months (up
491 to 15 µatm; Djeutchouang et al., 2022). The meridional coverage provided by the ‘zigzag’ runs
492 could explain why these runs generally outperform the ‘one-latitude’ runs in our study, and show
493 significant reduction in both RMSE and bias, even though the global pCO₂ data density is raised
494 by as little as 0.01-0.07 %.

495 The greatest reduction in mean bias out of all runs is shown by run ‘x13_10Y_W’ (**Figs.**
496 **5, 6d**), which represents ‘one-latitude’ ‘high-sampling’ (i.e., 25,395 observations) during southern
497 hemisphere winter months only. This sampling strategy seems thus to have a higher ability to
498 reduce the ML model’s tendency to overestimate pCO₂ in the Southern Ocean compared to any of
499 the meridional (‘zigzag’) runs. However, it should be noted that run ‘x13_10Y_W’ covers areas
500 south of 55° S (**Fig. S4**), and its improvement in mean bias (and mean RMSE) is particularly
501 prevalent at these high latitudes (e.g., **Figs. S7, S9, S12, S17**). Whether or not this run is, in fact,
502 feasible with current or future technology is uncertain as parts of the southernmost tracks
503 potentially cover the Southern Ocean ice zone (**Fig. S19**), and solar radiation for solar-powered
504 platforms and sensors becomes very limited during winter south of 55° S. Furthermore, this
505 particular sampling strategy requires 13 USVs, and so would be the most costly of the observing
506 scenarios. Although run ‘x13_10Y_W’ demonstrates the highest reduction in mean bias out of all
507 runs, the ‘zigzag’ runs still reduce mean bias in the Southern Ocean by 44-65 % (vs. 77 % for run
508 ‘x13_10Y_W’).

509 Overall, the ‘zigzag’ runs include significantly fewer observations, require fewer USVs,
510 collect samples over the same duration, or even half the time as run ‘x13_10Y_W’, cover areas
511 north of 55°S and within the ice-free zone, and show major improvement in the reconstruction of
512 pCO₂, attested to by reductions in both bias and RMSE. The ‘zigzag’ runs also closely match both
513 the global and Southern Ocean ‘model truth’ air-sea CO₂ flux for the duration of sample additions
514 (**Figs. 10, S18**). It also appears that the ‘zigzag’ runs generally have a greater impact on both the
515 pCO₂ reconstruction and the air-sea flux further back in time, starting to deviate from the ‘SOCAT-
516 baseline’ earlier compared to the ‘one-latitude’ runs (**Figs. 6, 9, 10, S9, S15, S17, S18**). Even the
517 ‘zigzag’ scenarios with the least number of USVs (e.g., ‘Z_x4_10Y_YR’) reduces Southern Ocean
518 reconstruction bias and RMSE by up to 46 % and 11 %, respectively, and could provide a basis
519 for realistic future Southern Ocean pCO₂ sampling campaigns.

520 The main motivation for improving surface ocean pCO₂ reconstructions is so that we can
521 more accurately estimate the current and future oceanic uptake of anthropogenic carbon. The
522 Southern Ocean is a significant carbon sink, but estimates of the air-sea CO₂ flux diverge
523 substantially in this region (Takahashi et al., 2009; Landschützer et al., 2014, 2015; Rödenbeck et
524 al., 2015; Williams et al., 2017; Gray et al., 2018; Gruber et al., 2019; Bushinsky et al., 2019; Long

525 et al., 2021; Fay and McKinley, 2021; Wu et al., 2022). Southern Ocean estimates incorporating
526 observations from biogeochemical floats have shown a significantly weaker sink compared to
527 those based only on observations from ships (Williams et al., 2017; Gray et al., 2018; Bushinsky
528 et al., 2019). Bushinsky et al. (2019) and Hauck et al. (2023) performed similar sampling
529 experiments as presented here, by comparing ML surface ocean pCO₂ reconstructions based on
530 SOCAT vs. additional SOCCOM or ideal virtual floats. These studies showed that SOCAT
531 sampling alone overestimates the CO₂ uptake in the Southern Ocean, and that additional floats
532 reduce this overestimation, leading to a decreased (weakened) ocean carbon sink. In contrast, we
533 find that the pCO₂-Residual method underestimates the CO₂ uptake with only SOCAT sampling,
534 and that adding USVs increased (strengthened) the Southern Ocean and global ocean sink by up
535 to 0.1 Pg C yr⁻¹ (**Figs. 10, S18; Table S2**).

536 Going forward, additional studies are needed to better understand why these results suggest
537 a different direction of the sink change with additional sampling. These differences could stem
538 from the use of different reconstruction methods assessed. Hauck et al. (2023) used the MPI-SOM-
539 FFN and CarboScope/Jena-MLS reconstruction methods, while we use the pCO₂-Residual
540 method. Another substantial difference between the studies is the models and numbers of ensemble
541 members used as the testbed. Hauck et al. (2023) use a single hindcast model, while we use 25
542 members each from three Earth System Models. We find substantial spread across these 75
543 members (**Figs. S8, S10, S14, S16**), indicating that model structure and internal variability
544 significantly impact results. Our study and Hauck et al. (2023) use different sampling masks and
545 approaches for the calculation of fluxes, which could also be a factor. Targeted, coordinated studies
546 using multiple reconstruction approaches with consistent testbed structures and experimental
547 approaches are clearly needed (Rödenbeck et al., 2015). Despite this need for this additional work,
548 studies do agree that additional Southern Ocean observations could significantly improve
549 reconstructions of air-sea CO₂ fluxes.

550 What else can we learn using the model testbed? The ‘SOCAT-baseline’ demonstrates a
551 weakening of the global and Southern Ocean carbon sink starting in the 1990s with a peak around
552 year 2000 (**Figs. 10, S18**), which is in broad agreement with various data products using real-world
553 SOCAT data (e.g., Gruber et al., 2019; Landschützer et al., 2015; Bushinsky et al., 2019;
554 Bennington et al., 2022; Gloege et al., 2022). Peaks in bias and RMSE coincide in time with the

555 weakening sink (**Figs. 6d, 9d**). As shown by **Figure 10**, this ‘low sink’ is significantly exaggerated
556 compared to the ‘model truth’. To better understand this discrepancy, we performed an additional
557 experiment based on run ‘Z_x10_5Y_YR’, but assumed sampling every year for the entire testbed
558 period (i.e., 1982-2016). There is now a significant reduction in the temporal variability of
559 reconstruction bias; with the additional 35-year USV sampling, the reconstructed Southern Ocean
560 air-sea CO₂ flux closely matches the ‘model truth’ for the entire testbed duration (**Fig. S20**). This
561 suggests that the large decadal variability of air-sea CO₂ fluxes since the 1980s, and the weak
562 anomaly in the Southern Ocean carbon sink in the early 2000s (Le Quéré et al., 2007; Landschützer
563 et al., 2015; Gruber et al., 2019; Bennington et al., 2022a,b; Friedlingstein et al., 2023), may be at
564 least partially attributable to undersampling of the Southern Ocean. This is in agreement with the
565 float sampling experiments performed by Hauck et al. (2023), attributing the strong decadal
566 variability to sparse and skewed SOCAT data distributions. We will further explore this issue in
567 future work. Still, this preliminary experiment suggests that interpretations of trends and variability
568 of the global and Southern Ocean carbon sink should be considered with caution.

569 **5. Conclusions**

570 By using the Large Ensemble Testbed (LET), we show that targeted meridional and winter
571 sampling in the Southern Ocean can improve global and Southern Ocean ML surface ocean pCO₂
572 reconstructions. Significant improvements are possible by raising the global pCO₂ data density by
573 as little as 0.01-0.07 %. Further, we find that this modest amount of additional Saildrone USV
574 sampling increases the global and Southern Ocean air-sea CO₂ flux by up to 0.1 Pg C yr⁻¹, a
575 quantity equivalent to 25 % of the uncertainty in the ocean carbon sink (0.4 Pg C yr⁻¹;
576 Friedlingstein et al., 2023). Our findings are consistent with previous studies suggesting that
577 additional observations during southern hemisphere winter months and covering meridional
578 gradients can reduce uncertainties and biases in the reconstructions (Lenton et al., 2006; Monteiro
579 et al., 2010; Djeutchouang et al., 2022; Mackay et al., 2022). As opposed to other autonomous
580 platform approaches, Saildrone USVs obtain in situ pCO₂ observations with uncertainties
581 equivalent to the highest-quality observations collected by research ships ($\pm 2 \mu\text{atm}$; Sabine et al.,
582 2020; Sutton et al., 2021), and can operate at a high speed so that the spatial extent and seasonal
583 cycle of meridional gradients can be covered. The approach of combining high-accuracy Saildrone
584 USV and SOCAT observations represents thus a promising solution to improve future surface

585 ocean pCO₂ reconstructions and the accuracy of the ocean carbon sink. Lastly, we show that the
586 large variability in bias, and the weakening of the global and Southern Ocean carbon sink in the
587 2000s, may be partially an artefact of Southern Ocean undersampling.

588 **Code availability**

589 Data analysis scripts will be made available in a GitHub repository upon publication.

590 **Data availability**

591 The Large Ensemble Testbed is publicly available at
592 https://figshare.com/collections/Large_ensemble_pCO2_testbed/4568555.

593

594 **Author contribution**

595 THH, GAM and AJS designed the experiments, and THH performed the simulations. THH, ARF
596 and LG developed the code. THH and ARF calculated the air-sea fluxes. THH prepared the
597 manuscript with contributions from all co-authors.

598 **Competing interests**

599 The authors declare that they have no conflict of interest.

600 **Acknowledgements**

601 We acknowledge funding from NOAA through the Climate Observations and Monitoring Program
602 (Award #NA20OAR4310340) and from NSF through the LEAP STC (Award #2019625). This is
603 PMEL contribution 5549. We would also like to acknowledge and thank Val Bennington, Julius
604 Busecke, Devan Samant and Abby Shaum for providing technical support, and Viviana Acquaviva
605 for discussions regarding the manuscript. Lastly, we wish to thank two anonymous reviewers,
606 whose contributions greatly improved the manuscript.

607

608 **References**

609

610 Bakker, D. C. E., Pfeil, B., Landa, C. S., Metzl, N., O'Brien, K. M., Olsen, A., Smith, K., Cosca,
611 C., Harasawa, S., Jones, S. D., Nakaoka, S., Nojiri, Y., Schuster, U., Steinhoff, T., Sweeney, C.,
612 Takahashi, T., Tilbrook, B., Wada, C., Wanninkhof, R., Alin, S. R., Balestrini, C. F., Barbero, L.,
613 Bates, N. R., Bianchi, A. A., Bonou, F., Boutin, J., Bozec, Y., Burger, E. F., Cai, W.-J., Castle, R.
614 D., Chen, L., Chierici, M., Currie, K., Evans, W., Featherstone, C., Feely, R. A., Fransson, A.,
615 Goyet, C., Greenwood, N., Gregor, L., Hankin, S., Hardman-Mountford, N. J., Harlay, J., Hauck,
616 J., Hoppema, M., Humphreys, M. P., Hunt, C. W., Huss, B., Ibáñez, J. S. P., Johannessen, T.,
617 Keeling, R., Kitidis, V., Körtzinger, A., Kozyr, A., Krasakopoulou, E., Kuwata, A., Landschützer,
618 P., Lauvset, S. K., Lefèvre, N., Lo Monaco, C., Manke, A., Mathis, J. T., Merlivat, L., Millero, F.
619 J., Monteiro, P. M. S., Munro, D. R., Murata, A., Newberger, T., Omar, A. M., Ono, T., Paterson,
620 K., Pearce, D., Pierrot, D., Robbins, L. L., Saito, S., Salisbury, J., Schlitzer, R., Schneider, B.,
621 Schweitzer, R., Sieger, R., Skjelvan, I., Sullivan, K. F., Sutherland, S. C., Sutton, A. J., Tadokoro,
622 K., Telszewski, M., Tuma, M., van Heuven, S. M. A. C., Vandemark, D., Ward, B., Watson, A.
623 J., and Xu, S.: A multi-decade record of high-quality $f\text{CO}_2$ data in version 3 of the Surface Ocean
624 CO_2 Atlas (SOCAT), *Earth System Science Data*, 8, 383–413, [https://doi.org/10.5194/essd-8-383-](https://doi.org/10.5194/essd-8-383-2016)
625 [2016](https://doi.org/10.5194/essd-8-383-2016), 2016.

626 Bakker, D. C. E., Alin, S. R., Becker, M., Bittig, H. C., Castaño-Primo, R., Feely, R. A., Gkritzalis,
627 T., Kadono, K., Kozyr, A., Lauvset, S. K., Metzl, N., Munro, D. R., Nakaoka, S., Nojiri, Y., O'Brien,
628 K. M., Olsen, A., Pfeil, Benjamin, P., Denis, S., Tobias, S., Kevin F., Sutton, A. J., Sweeney, C.,
629 Tilbrook, B., Wada, C., Wanninkhof, R., Willstrand W. A., Akl, J., Apelthun, L. B., Bates, N.,
630 Beatty, C. M., Burger, E. F., Cai, W., Cosca, C. E., Corredor, J. E., Cronin, M., Cross, J. N., De
631 Carlo, E. H., DeGrandpre, M. D., Emerson, S. R., Enright, M. P., Enyo, K., Evans, W., Frangoulis,
632 C., Fransson, A., García-Ibáñez, M. I., Gehrung, M., Giannoudi, L., Glockzin, M., Hales, B.,
633 Howden, S. D., Hunt, C. W., Ibáñez, J. S. P., Jones, S. D., Kamb, L., Körtzinger, A., Landa, C.
634 S., Landschützer, P., Lefèvre, N., Lo Monaco, C., Macovei, V. A., Maenner J. S., Meinig, C.,
635 Millero, F. J., Monacci, N. M., Mordy, C., Morell, J. M., Murata, A., Musielewicz, S., Neill, .,
636 Newberger, T., Nomura, D., Ohman, M., Ono, T., Passmore, A., Petersen, W., Petihakis, G.,
637 Perivoliotis, L., Plueddemann, A. J., Rehder, G., Reynaud, T., Rodriguez, C., Ross, A. C.,
638 Rutgersson, A., Sabine, C. L., Salisbury, J. E., Schlitzer, R., Send, U., Skjelvan, I., Stamatakis, N.,
639 Sutherland, S. C., Sweeney, C., Tadokoro, K., Tanhua, T., Telszewski, M., Trull, T., Vandemark,
640 D., van Ooijen, E., Voynova, Y. G., Wang, H., Weller, R. A., Whitehead, C., Wilson, D.: Surface

641 Ocean CO₂ Atlas Database Version 2022 (SOCATv2022) (NCEI Accession 0253659), NOAA
642 National Centers for Environmental Information [dataset], <https://doi.org/10.25921/1h9f-nb73>,
643 2022.

644 Behncke, J., Landschützer, P. & Tanhua, T. A detectable change in the air-sea CO₂ flux estimate
645 from sailboat measurements. *Scientific Reports*, 14, 3345, [https://doi.org/10.1038/s41598-024-](https://doi.org/10.1038/s41598-024-53159-0)
646 [53159-0](https://doi.org/10.1038/s41598-024-53159-0), 2024.

647 Bennington, V., Galjanic, T., and McKinley, G. A.: Explicit Physical Knowledge in Machine
648 Learning for Ocean Carbon Flux Reconstruction: The pCO₂-Residual Method, *Journal of*
649 *Advances in Modeling Earth Systems*, 14(10), <https://doi.org/10.1029/2021ms002960>, 2022a.

650 Bennington, V., Gloege, L., and McKinley, G. A.: Variability in the global ocean carbon sink from
651 1959 to 2020 by correcting models with observations, *Geophysical Research Letters*, 49(14),
652 <https://doi.org/10.1029/2022GL098632>, (2022b).

653 Bushinsky, S. M., Landschützer, P., Rödenbeck, C., Gray, A. R., Baker, D., Mazloff, M. R.,
654 Resplandy, L., Johnson, K. S., and Sarmiento, J. L.: Reassessing Southern Ocean air-sea CO₂ flux
655 estimates with the addition of biogeochemical float observations, *Global Biogeochemical Cycles*,
656 33(11), 1370-1388, <https://doi.org/10.1029/2019GB006176>, 2019.

657 Chen, T., and Guestrin, C.: Xgboost: A scalable tree boosting system, In: *Proceedings of the 22nd*
658 *ACM SIGKDD international conference on knowledge discovery and data mining* (pp. 785-794),
659 <https://doi.org/10.1145/2939672.2939785>, 2016.

660 Denvil-Sommer, A., Gehlen, M., and Vrac, M.: Observation system simulation experiments in the
661 Atlantic Ocean for enhanced surface ocean pCO₂ reconstructions, *Ocean Science*, 17, 1011-1030,
662 <https://doi.org/10.5194/os-17-1011-2021>, 2021.

663 Deser, C., Phillips, A., Bourdette, V., and Teng, H.: Uncertainty in climate change projections: the
664 role of internal variability, *Climate Dynamics*, 38, 527-546, [https://doi.org/10.1007/s00382-010-](https://doi.org/10.1007/s00382-010-0977-x)
665 [0977-x](https://doi.org/10.1007/s00382-010-0977-x), 2012

666 Djeutchouang, L. M., Chang, N., Gregor, L., Vichi, M., and Monteiro, P. M. S.: The sensitivity of
667 pCO₂ reconstructions to sampling scales across a Southern Ocean sub-domain: a semi-idealized

668 ocean sampling simulation approach, *Biogeosciences*, 19, 4171-4195, <https://doi.org/10.5194/bg->
669 [19-4171-2022](https://doi.org/10.5194/bg-19-4171-2022), 2022

670 Fay, A. R., Lovenduski, N. S., McKinley, G. A., Munro, D. R., Sweeney, C., Gray, A. R.,
671 Landschützer, P., Stephens, B. B., Takahashi, T., and Williams, N.: Utilizing the Drake Passage
672 Time-series to understand variability and change in subpolar Southern Ocean pCO₂,
673 *Biogeosciences*, 15(12), 3841-3855, <https://doi.org/10.5194/bg-15-3841-2018>, 2018.

674 Fay, A. R., and McKinley, G. A.: Observed regional fluxes to constrain modeled estimates of the
675 ocean carbon sink, *Geophysical Research Letters*, 48(20), <https://doi.org/10.1029/2021GL095325>,
676 2021.

677

678 Friedlingstein, P., O'Sullivan, M., Jones, M. W., Andrew, R. M., Bakker, D. C. E., Hauck, J.,
679 Landschützer, P., Le Quéré, C., Luijkx, I. T., Peters, G. P., Peters, W., Pongratz, J., Schwingshackl,
680 C., Sitch, S., Canadell, J. G., Ciais, P., Jackson, R. B., Alin, S. R., Anthoni, P., Barbero, L., Bates,
681 N. R., Becker, M., Bellouin, N., Decharme, B., Bopp, L., Brasika, I. B. M., Cadule, P.,
682 Chamberlain, M. A., Chandra, N., Chau, T.-T.-T., Chevallier, F., Chini, L. P., Cronin, M., Dou,
683 X., Enyo, K., Evans, W., Falk, S., Feely, R. A., Feng, L., Ford, D. J., Gasser, T., Ghattas, J.,
684 Gkritzalis, T., Grassi, G., Gregor, L., Gruber, N., Gürses, Ö., Harris, I., Hefner, M., Heinke, J.,
685 Houghton, R. A., Hurtt, G. C., Iida, Y., Ilyina, T., Jacobson, A. R., Jain, A., Jarníková, T., Jersild,
686 A., Jiang, F., Jin, Z., Joos, F., Kato, E., Keeling, R. F., Kennedy, D., Klein Goldewijk, K., Knauer,
687 J., Korsbakken, J. I., Körtzinger, A., Lan, X., Lefèvre, N., Li, H., Liu, J., Liu, Z., Ma, L., Marland,
688 G., Mayot, N., McGuire, P. C., McKinley, G. A., Meyer, G., Morgan, E. J., Munro, D. R., Nakaoka,
689 S.-I., Niwa, Y., O'Brien, K. M., Olsen, A., Omar, A. M., Ono, T., Paulsen, M., Pierrot, D., Pockock,
690 K., Poulter, B., Powis, C. M., Rehder, G., Resplandy, L., Robertson, E., Rödenbeck, C., Rosan, T.
691 M., Schwinger, J., Séférian, R., Smallman, T. L., Smith, S. M., Sospedra-Alfonso, R., Sun, Q.,
692 Sutton, A. J., Sweeney, C., Takao, S., Tans, P. P., Tian, H., Tilbrook, B., Tsujino, H., Tubiello, F.,
693 van der Werf, G. R., van Ooijen, E., Wanninkhof, R., Watanabe, M., Wimart-Rousseau, C., Yang,
694 D., Yang, X., Yuan, W., Yue, X., Zaehle, S., Zeng, J., and Zheng, B.: Global Carbon Budget 2023,
695 *Earth Syst. Sci. Data*, 15, 5301–5369, <https://doi.org/10.5194/essd-15-5301-2023>, 2023.

696 Fyfe, J. C., Derksen, C., Mudryk, L., Flato, G. M., Santer, B. D., Swart, N. C., Molotch, N. P.,
697 Zhang, X., Wan, H., Arora, V. K., Scinocca, J., and Jiao, Y.: Large near-term projected snowpack
698 loss over the western United States, *Nature communications*, 8(1), 14996,
699 <https://doi.org/10.1038/ncomms14996>, 2017.

700 Gloege, L., McKinley, G. A., Landschützer, P., Fay, A. R., Frolicher, T. L., and Fyfe, J. C.:
701 Quantifying Errors in Observationally Based Estimates of Ocean Carbon Sink Variability, *Global*
702 *Biogeochemical Cycles*, 35(4), <https://doi.org/10.1029/2020gb006788>, 2021.

703 Gloege, L., Yan, M., Zheng, T. and McKinley, G. A.: Improved quantification of ocean carbon
704 uptake by using machine learning to merge global models and pCO₂ data, *Journal of Advances in*
705 *Modeling Earth Systems*, 14(2), <https://doi.org/10.1029/2021MS002620>, 2022.

706

707 Good, S. A., Martin, M., and Rayner, N. A.: EN4: Quality controlled ocean temperature and
708 salinity profiles and monthly objective analyses with uncertainty estimates, *Journal of*
709 *Geophysical Research Oceans*, 118(12), 6704-6717, <https://doi.org/10.1002/2013JC009067>,
710 2013.

711

712 Gray, A. R., Johnson, K. S., Bushinsky, S. M., Riser, S. C., Russell, J. L., Talley, L. D.,
713 Wanninkhof, R., Williams, N. L., and Sarmiento, J. L.: Autonomous biogeochemical floats detect
714 significant carbon dioxide outgassing in the high-latitude Southern Ocean, *Geophysical Research*
715 *Letters*, 45(17), 9049-9057, <https://doi.org/10.1029/2018GL078013>, 2018.

716 Gregor, L., Lebehot, A. D., Kok, S., and Monteiro, P. M. S.: A comparative assessment of the
717 uncertainties of global surface ocean CO₂ estimates using a machine-learning ensemble (CSIR-
718 ML6 version 2019a) – have we hit the wall?, *Geoscientific Model Development*, 12, 5113-5136,
719 <https://doi.org/10.5194/gmd-12-5113-2019>, 2019.

720 Gregor, L. and Fay, A. R.: Air-sea CO₂ fluxes for surface pCO₂ data products using a standardized
721 approach, Zenodo [code], <https://doi.org/10.5281/zenodo.5482547>, 2021.

722 Gruber, N., Landschützer, P., and Lovenduski, N. S.: The variable Southern Ocean carbon sink,
723 *The Annual Review of Marine Science*, 11, 159-86, [https://doi.org/10.1146/annurev-marine-](https://doi.org/10.1146/annurev-marine-121916-063407)
724 [121916-063407](https://doi.org/10.1146/annurev-marine-121916-063407), 2019.

725 Hauck, J., Nissen, C., Landschützer, P., Rödenbeck, C., Bushinsky, S., and Olsen, A.: Sparse
726 observations induce large biases in estimates of the global ocean CO₂ sink: and ocean model
727 subsampling experiment, *Philosophical Transactions Of the Royal Society A*, 381:20220063,
728 <https://doi.org/10.1098/rsta.2022.0063>, 2023.

729 Kay, J. E., Deser, C., Phillips, A., Mai, A., Hannay, C., Strand, G., Arblaster, J. M., Bates, S. C.,
730 Danabasoglu, G., Edwards, J., Holland, M., Kushner, P., Lamarque, J-F., Lawrence, D., Lindsay,
731 K., Middelton, A., Munoz, E., Neale, R., Oleson, K., Polvani, L., and Vertenstein, M.: The
732 Community Earth System Model (CESM) large ensemble project: A community resource for
733 studying climate change in the presence of internal climate variability, *Bulletin of the American*
734 *Meteorological Society*, 96(8), 1333-1349, <https://doi.org/10.1175/BAMS-D-13-00255>, 2015.

735 Khatiwala, S., Primeau, F., and Hall., T.: Reconstruction of the history of anthropogenic CO₂
736 concentrations in the ocean, *Nature*, 462(7271), 346-349, <https://doi.org/10.1038/nature08526>,
737 2009.

738 Landschützer, P., Gruber, N., Bakker, D. C. E., and Schuster, U.: Recent variability of the global
739 ocean carbon sink, *Global Biogeochemical Cycles*, 28(9), 927-949,
740 <https://doi.org/10.1002/2014GB004853>, 2014.

741 Landschützer, P., Gruber, N., Haumann, F. A., Rödenbeck, C., Bakker, D. C. E., Van Heuven, S.,
742 Hoppema, M., Metzl, N., Sweeney, C., Takahashi, T., Brook, B., and Wanninkhof, R.: The
743 reinvigoration of the Southern Ocean carbon sink, *Science*, 349(6253), 1221-1224,
744 <https://doi.org/10.1126/science.aab2620>, 2015.

745 Landschützer, P., Tanhua, T., Behncke, J., and Keppler, L.: Sailing through the Southern Ocean
746 seas of air-sea CO₂ flux uncertainty, *Philosophical Transactions of the Royal Society A*, 381,
747 <https://doi.org/10.1098/rsta.2022.0064>, 2023.

748 Lenton, A. B., Matear, R. J., and Tilbrook, B.: Design of an observational strategy for quantifying
749 the Southern Ocean uptake of CO₂, *Global Biogeochemical Cycles*, 20, 1-11.
750 <https://doi.org/10.1029/2005GB002620>, 2006.

751 Lenton, A. B., Tilbrook, B., Law, R. M., Bakker, D. C. E., Doney, S. C., Gruber, N., Ishii, M.,
752 Hoppema, M., Lovenduski, N. S., Matear, R. J., McNeil. B. I., Metzl, N., Mikaloff Fletcher, S. E.,

753 Monteiro, P. M. S., Rödenbeck, C., Sweeney, C., and Takahashi, T.: Sea-air CO₂ fluxes in the
754 Southern Ocean for the period 1990-2009, *Biogeosciences*, 10, 4037-4054,
755 <https://doi.org/10.5194/bg-10-4037-2013>, 2013.

756 Le Quéré, C., Rödenbeck, C., Buitenhuis, E. T., Conway, T. J., Lagenfelds, R., Gomez, A.,
757 Labuschagne C., Ramonet, M., Nakazawa, T., Metzl, N., Gillett, N., and Heimann, M.: Saturation
758 of the Southern Ocean CO₂ sink due to recent climate change, *Science*, 316(5832), 1735-1738,
759 <https://doi.org/10.1126/science.1136188>, 2007.

760 Long, M. C., Stephens, B. B., McKain, K., Sweeney, C., Keeling, R. F., Kort, E. A., Morgan, E.
761 J., Bent, J. D., Chandra, N., Chevallier, F., Commane, R., Daube, B. C., Krummel, P. B., Loh, Z.,
762 Luijkx, I. T., Munro, D., Patra, P., Peters, W., Ramonet, M., Rödenbeck, C., Stavert, A., Tans, P.,
763 and Wofsy, S. C.: Strong Southern Ocean carbon uptake evident in airborne observations, *Science*,
764 374(6572), 1275-1280, <https://doi.org/10.1126/science.abi4355>, 2021.

765 Mackay, N., and Watson, A.: Winter air-sea CO₂ fluxes constructed from summer observations of
766 the polar Southern Ocean suggest weak outgassing, *Journal of Geophysical Research: Oceans*,
767 126(5), e2020JC016600, <https://doi.org/10.1029/2020JC016600>, 2021.

768 Mackay, N., Watson, A., Suntharalingam, P., Chen, Z., and Rödenbeck, C.: Improved winter data
769 coverage of the Southern Ocean CO₂ sink from extrapolation of summertime observations,
770 *Communications Earth & Environment*, 3, 265, <https://doi.org/10.1038/s43247-022-00592-6>,
771 2022.

772 McKinley, G. A., Fay, A. R., Eddebbar, Y. A., Gloege, L., and Lovenduski, N. S.: External forcing
773 explains recent decadal variability of the ocean carbon sink, *AGU Advances*, 1(2),
774 e2019AV000149, <https://doi.org/10.1029/2019AV000149>, 2020.

775 Mongwe, N. P., Vichi, M., and Monteiro, P. M. S.: The seasonal cycle of *p*CO₂ and CO₂ fluxes in
776 the Southern Ocean: diagnosing anomalies in CMIP5 Earth system models, *Biogeosciences*, 15(9),
777 2851-2872, <https://doi.org/10.5194/bg-15-2851-2018>, 2018.

778 Monteiro, P. M. S., Gregor, L., Lévy, M., Maenner, S., Sabine, C. L., and Swart, S.: Intraseasonal
779 variability linked to sampling alias in air-sea CO₂ fluxes in the Southern Ocean, *Geophysical*
780 *Research Letters*, 42(20), 8507-8514, <https://doi.org/10.1002/2015GL066009>, 2015.

781 Rodgers, K. B., Lin, J., and Frölicher, T. L.: Emergence of multiple ocean ecosystem drivers in a
782 large ensemble suite with an Earth system model, *Biogeosciences*, 12(11), 3301-3320.
783 <https://doi.org/10.5194/bg-12-3301-2015>, 2015.

784 Rödenbeck, C., Bakker, D. C. E., Gruber, N., Iida, Y., Jacobson, A. R., Jones, S., Landschützer,
785 P., Metzl, N., Nakaoka, S., Olsen, A., Park, G.-H., Peylin, P., Rodgers, K. B., Sasse T. P., Schuster,
786 U., Shutler, J. D., Valsala, V., Wannikkhof, R., and Zeng, J.: Data-based estimates of the ocean
787 carbon sink variability – first results of the Surface Ocean $p\text{CO}_2$ Mapping intercomparison
788 (SOCOM), *Biogeosciences*, 12, 7251-7278, <https://doi.org/10.5194/bg-12-7251-2015>, 2015.

789 Sabine, C., Sutton, A., McCabe, K., Lawrence-Slavas, N., Alin, S, Feely, R., Jenkins, R., Maenner,
790 S., Meinig, C., Thomas, J., van Ooijen, E., Passmore, A., and Tilbrook, B.: Evaluation of a new
791 carbon dioxide system for autonomous surface vehicles, *Journal of Atmospheric and Oceanic*
792 *Technology*, 37(8), 1305-1317, <https://doi.org/10.1175/JTECH-D-20-0010.1>, 2020.

793 Stamell, J., Rustagi, R. R., Gloege, L., and McKinley, G. A.: Strengths and weaknesses of three
794 Machine Learning methods for $p\text{CO}_2$ interpolation, *Geoscientific Model Development*
795 *Discussions*[preprint], doi:10.5194/gmd-2020-311, 22 October 2020.

796 Sutton, A. J., Williams, N. L., and Tilbrook, B.: Constraining Southern Ocean CO_2 flux uncertainty
797 using uncrewed surface vehicle observations, *Geophysical Research Letters*, 48(3),
798 e2020GL091748, <https://doi.org/10.1029/2020GL091748>, 2021.

799 Takahashi, T., Olafsson, J., Goddard, J. G., Chipman, D. W., and Sutherland, S. C.: Seasonal
800 variation of CO_2 and nutrients in the high-latitude surface oceans: A comparative study, *Global*
801 *Biogeochemical Cycles*, 7(4), 843-878, <https://doi.org/10.1029/93GB02263>, 1993.

802 Takahashi, T., Sutherland, S. C., Wanninkhof, R., Sweeney, C., Feely, R. A., Chipman, D. W.,
803 Hales, B., Friederich, G., Chavez, F., Sabine, C., Watson, A., Bakker, D. C. E., Schuster, U., Metzl,
804 N., Yoshikawa-Inoue, H., Ishii, M., Midorikawa, T., Nojiri, Y., Körtzinger, A., Steinhoff, T.,
805 Hoppema, M., Olafsson, J., Arnarson, T. S., Tilbrook, B., Johannessen, T., Olsen, A., Bellerby,
806 R., Wong, C. S., Delille, B., Bates, N. R., and de Baar, H. J. W.: Climatological mean and decadal
807 change in surface ocean $p\text{CO}_2$, and net sea-air CO_2 flux over the global oceans, *Deep Sea Research*

808 Part II: Topical Studies in Oceanography, 56(8-10), 554-557,
809 <https://doi.org/10.1016/j.dsr2.2008.12.009>, 2009.

810 Toms, B. A., Barnes, E. A., and Ebert-Uphoff, I.: Physically interpretable neural networks for the
811 geosciences: Applications to earth system variability, Journal of Advances in Modeling Earth
812 Systems, 12(9), e2019MS002002, <https://doi.org/10.1029/2019MS002002>, 2020.

813 Williams, N. L., Juranek, L. W., Feely, R. A., Johnson, K. S., Sarmiento, J. L., Talley, L. D.,
814 Dickson, A. G., Gray, A. R., Wannikhof, R., Russell, J. L., Riser, S. C., and Takeshita, Y.:
815 Calculating surface ocean pCO₂ from biogeochemical Argo floats equipped with pH: An
816 uncertainty analysis, Global Biogeochemical Cycles, 31(3), 591-604,
817 <https://doi.org/10.1002/2016GB005541>, 2017.

818 Wu, Y., Bakker, D. C. E., Achterberg, E. P., Silva, A. N., Pickup D. P., Li, X., Hartman, S.,
819 Stappard, D., Qi, D., and Tyrrell, T.: Integrated analysis of carbon dioxide and oxygen
820 concentrations as a quality control of ocean float data, Communications Earth & Environment, 3,
821 92, <https://doi.org/10.1038/s43247-022-00421-w>, 2022.

822

823

824

825

826

827